Improvements to the Geostationary Visible Imager Ray-Matching Calibration Algorithm for CERES Edition 4

DAVID R. DOELLING

Climate Science Branch, NASA Langley Research Center, Hampton, Virginia

CONOR O. HANEY, BENJAMIN R. SCARINO, ARUN GOPALAN, AND RAJENDRA BHATT

Science Systems and Applications, Inc., Hampton, Virginia

(Manuscript received 1 June 2016, in final form 9 September 2016)

ABSTRACT

The Clouds and the Earth's Radiant Energy System (CERES) project relies on geostationary imager–derived TOA broadband fluxes and cloud properties to account for the regional diurnal fluctuations between the *Terra* and *Aqua* CERES and MODIS measurements. The CERES project employs a ray-matching calibration algorithm in order to transfer the *Aqua* MODIS calibration to the geostationary (GEO) imagers, thereby allowing the derivation of consistent fluxes and cloud retrievals across the 16 GEO imagers utilized in the CERES record. The CERES Edition 4 processing scheme grants the opportunity to recalibrate the GEO record using an improved GEO/MODIS all-sky ocean ray-matching algorithm. Using a graduated angle matching method, which is most restrictive for anisotropic clear-sky ocean radiances and least restrictive for isotropic bright cloud radiances, reduces the bidirectional bias while preserving the dynamic range. Furthermore, SCIAMACHY hyperspectral radiances are used to account for both the solar incoming and Earth-reflected spectra in order to correct spectral band differences. As a result, the difference between the linear regression offset and the maintained GEO space count was reduced, and the calibration slopes computed from the linear fit and the regression through the space count agreed to within 0.4%. A deep convective cloud (DCC) ray-matching algorithm is also presented. The all-sky ocean and DCC ray-matching timeline gains are within 0.7% of one another. Because DCC are isotropic and the brightest, Earth targets with near-uniform visible spectra, the temporal standard error of GEO imager gains, are reduced by up to 60% from that of all-sky ocean targets.

1. Introduction

The Clouds and the Earth's Radiant Energy System (CERES; Wielicki et al. 1996) project synoptic 1° latitude × 1° longitude gridded (SYN1deg) product relies on geostationary imager–derived TOA broadband fluxes and retrieved cloud properties to account for the regional diurnal fluctuations between the CERES and Moderate Resolution Imaging Spectroradiometer (MODIS) measurements (Doelling et al. 2013a). The cloud properties are also used to compute the hourly surface fluxes contained in the SYN1deg product (Rutan et al. 2015). The CERES and MODIS instruments are on board the *Terra* and *Aqua* sun-synchronous satellites, which have a 1030 and 1330 ECT, respectively. Similarly, the CERES and Visible Infrared Imaging Radiometer Suite (VIIRS) instruments on board the *Suomi-NPP*, and the future follow-on Joint Polar Satellite System (JPSS) satellites, are/will be in a 1330 ECT orbit. All of the 16 geostationary (GEO) imagers utilized by CERES between March 2000 and June 2015 lack an onboard visible calibration reference. Therefore, in order to derive consistent GEO-derived broadband fluxes and cloud properties, the GEO visible imager calibration is referenced to the MODIS band 1 (0.65 μm) calibration. The CERES GEO visible calibration relies on MODIS to account for sensor temporal degradation, as well as serve as an absolute on-orbit calibration reference. CERES employs GEO and MODIS ray-matched, or line of sight, coincident radiance pairs to transfer the MODIS calibration to the GEO visible imagers (Morstad et al. 2011; Doelling et al. 2013a).

Corresponding author address: David Doelling, NASA Langley Research Center, Bldg. 1250, Mail Stop 420, Hampton, VA 23681-2199. E-mail: david.r.doelling@nasa.gov

DOI: 10.1175/JTECH-D-16-0113.1

The advantage of MODIS/GEO ray matching is that the entire dynamic range of GEO-observed Earth-viewed radiances can be compared against MODIS in order to evaluate the linearity of the GEO visible imager response. For example, a nonlinear feature in the *Multifunctional Transport Satellite-1R* (*MTSAT-1R*) imager visible sensor response was detected using MODIS/*MTSAT-1R* ray matching, and was subsequently corrected by redefining the pixel point spread function (Doelling et al. 2015a; Khlopenkov et al. 2015). Furthermore, the Advanced Very High Resolution Radiometer (AVHRR)/3 sensor low and high gain ratio relationship was verified using *Meteosat-8* ray-matched radiances (Doelling et al. 2007). Any recently launched GEO can be rapidly calibrated and evaluated for linearity with this technique because there is usually sufficient ray-match sampling encompassing the entire dynamic range within one month after commissioning (Minnis et al. 2002).

GEO imagers can be ray matched against all sun-synchronous low-Earth-orbiting (LEO) satellite sensors because GEO imagers continuously scan on a set schedule. This attribute allows the GEO sensor to be used as a calibration transfer radiometer between LEO sensors. For example, Meirink et al. (2013) demonstrates that *Meteosat-8* or *-9* can be used as a calibration transfer radiometer to calibrate AVHRR with MODIS. Also, Doelling et al. (2015b) showed consistent *Terra* MODIS and *Aqua* MODIS band 1 relative calibration differences from nine GEOs, which were used as calibration transfer radiometers.

The GEO two-channel cloud retrieval algorithm for CERES Edition 3 (Ed3) requires equivalent MODIS-like 0.65-μm radiances and IR-channel temperatures (Minnis et al. 1994). This approach is applicable to any GEO imager. Only the solar incoming radiance between the MODIS and GEO visible spectral bands are accounted for in Edition 3. For Edition 4, CERES employs a MODIS-like multichannel cloud retrieval code that is specific to each GEO. This requires that the MODIS/GEO ray-matched calibration take into account spectral band differences. The Earth-reflected spectral radiance is a function of both the solar incoming spectral irradiance and the reflective/absorptive properties of the surface, cloud, and atmospheric column. CERES Edition 4 uses spectral band adjustment factors (SBAF) derived from Scanning Imaging Absorption Spectrometer for Atmospheric Chartography (SCIAMACHY) hyperspectral footprint radiances convolved with the MODIS and GEO spectral response functions (SRF) over the ray-matching domains.

Another way to reduce the spectral difference uncertainty is to perform ray matching over deep convective clouds (DCC), which require the smallest spectral correction of all Earth-viewed scenes given that DCC spectral reflectance is nearly constant for wavelengths less than 1 μm (Doelling et al. 2013b; Vermote and Kaufman 1995). Ray matching over DCC has other advantages as well. For example, DCC are optically thick high-altitude clouds that are nearly isotropic for near-nadir viewing and solar conditions, thereby allowing for greater angular matching tolerance. Furthermore, DCC are the brightest Earth targets and therefore provide the greatest ray-matched signal-to-noise ratios. However, because DCC occur infrequently and are not evenly distributed over the tropics, it is possible that some GEO ray-matching domains may not have sufficient sampling (Hong et al. 2008).

The GEO/MODIS ray-matching technique requires a delicate balance between sufficient sampling and matching precision (see the appendix). Too much angular tolerance may introduce a bias because sensor pair bidirectional effects may be present. Precise angular matching will require long time intervals in order to obtain sufficient sampling, thus making it difficult to monitor degradation. In section 2, an improved GEO/MODIS all-sky tropical ocean (ATO) ray-matching technique is presented that incorporates variable angle matching thresholds, SBAF application, and spatial homogeneity filters. A GEO/MODIS DCC ray-matching algorithm is presented in section 3. Section 4 highlights ATO and DCC ray-matching comparison results, and section 5 contains the conclusions. The improved ray-matching techniques presented in this article should provide consistent GEO-derived fluxes and cloud properties for CERES, as well as for the broader GEO community.

2. ATO ray matching

a. Edition 3

The CERES Edition 3 GEO/MODIS ray-matching algorithm has been improved upon over many years. The algorithm was initiated at the NASA Langley Research Center in the 1980s in application to the *Nimbus-7* and *Geostationary Operational Environmental Satellite-2* (*GOES-2*; Minnis and Harrison 1984). The algorithm was expanded to utilize AVHRR, the Along-Track Scanning Radiometer (ATSR-2), the Visible and Infrared Scanner (VIRS), and MODIS as reference sensors (Ayers et al. 1998; Nguyen et al. 1999, 2001; Minnis et al. 2002). Comparing the GEO ray-matched gains from two intercalibrated reference sensors validated the ray-matching algorithm (Nguyen et al. 2004; Doelling et al. 2004). Ray-matching for calibration purposes is well established in the International Satellite Cloud Climatology Project (ISCCP), for which

AVHRR is used as the calibration reference (Desormeaux et al. 1993; Brest et al. 1997). Recently, the ISCCP B1U GEO record has been recalibrated by referencing the AVHRR Pathfinder Atmospheres–Extended (PATMOS-x) standard (Heidinger et al. 2010; Inamdar and Knapp 2015).

The CERES Edition 3 GEO/MODIS ray-matching technique follows the approach of Minnis et al. (2002), using *Terra* MODIS band 1 (0.65 μm) Collection 5 (C5) level 1B (L1B) as the calibration reference. Edition 4 will use *Aqua* MODIS band 1 C6 as the calibration reference, because it is the better-characterized MODIS instrument (Wu et al. 2013). For this study, Edition 3 results are also referenced to *Aqua* MODIS C6 for validation purposes. Over the GEO ATO domain, the GEO imager pixel-level counts (proportional to radiance), which are obtained from Man Computer Interactive Data Access System (McIDAS) servers (Lazzara et al. 1999), and *Aqua* MODIS C6 L1B radiances are averaged onto a 0.5° longitude × 0.5° latitude grid, provided that the measurements are coincident within 15 min. The GEO grid domain encompasses ±20°E/W and ±15°N/S from the GEO subsatellite location. Because land scenes have diverse spectral signatures, only ocean regions are considered. Furthermore, regions containing sun glint are excluded. The viewing zenith angle (VZA) and relative azimuthal angle (RAA) are each matched within 15°. Views in direct backscatter (RAA > 170°) or forward scatter (RAA < 10°) are avoided. The GEO radiance ($\mathrm{Rad_{GEO}}$) is linearly proportional to the GEO count (C) after subtracting the space count (C_0),

$$\mathrm{Rad_{GEO}} = \mathrm{gain}(C - C_0). \tag{1}$$

For second-generation GEO imagers—that is, *GOES-8–15* and *Meteosat-8–11*—a space clamp is used to maintain a constant space view count, which otherwise may vary under changing thermal conditions. The maintained C_0 for *GOES-8–15* is 29 (Weinreb et al. 1997) and for *Meteosat 8–11* C_0 is 51 (Govaerts and Clerici 2004). These values can be computed by observing either deep space or the unlit Earth disc. For this study, the long-term C_0 for *Meteosat-7* and *MTSAT-2* was found to be 4.95 and 1, respectively, based on the latter technique.

The reflectance (Ref) can be computed from the radiance (Rad),

$$\mathrm{Ref} = \mathrm{Rad}/[\mathrm{SC}\gamma(d)\mu_0], \tag{2}$$

where μ_0 is the cosine of the solar zenith angle (SZA), $\gamma(d)$ is an Earth–sun distance correction factor as a function of day of year, and SC is the band solar constant ($\mathrm{W\,m^{-2}\,sr^{-1}\,\mu m^{-1}}$). The SC is defined as

$$\mathrm{SC} = (\Sigma E_\lambda \mathrm{SRF}_\lambda \Delta_\lambda)/(\Sigma \mathrm{SRF}_\lambda \Delta_\lambda), \tag{3}$$

where E_λ is the incoming solar spectral radiance and SRF is the normalized spectral response function. The GEO radiances are ray matched with the *Aqua* MODIS L1B–calibrated radiances ($\mathrm{Rad_{MODIS}}$). The MODIS L1B product uses the MODIS Characterization Support Team (MCST) solar spectra (Guenther et al. 2002; ftp://mcst.ssaihq.com/pub/permanent/MCST/Solar_Irradiance/) to convert the MODIS reflectance values to radiances. Therefore, the CERES GEO SC is also computed using the MCST solar spectra.

b. SC ratio

The CERES Edition 3 CERES GEO ray-matching calibration algorithm produces MODIS-equivalent visible radiances. The algorithm assumes that the GEO reflectance ($\mathrm{Ref_{GEO}}$) should equal the angle-matched MODIS reflectance ($\mathrm{Ref_{MODIS}}$),

$$\mathrm{Ref_{GEO}} \equiv \mathrm{Ref_{MODIS}}. \tag{4}$$

By converting the Eq. (4) reflectances to radiances using Eq. (2), the MODIS-predicted ray-matched $\mathrm{Rad_{GEO}}$ is written as

$$\mathrm{Rad_{GEO}} = \mathrm{Rad_{MODIS}}(\mathrm{SC_{GEO}}/\mathrm{SC_{MODIS}})(\mu_{0\mathrm{GEO}}/\mu_{0\mathrm{MODIS}}). \tag{5}$$

The SC ratio is defined by the ($\mathrm{SC_{GEO}}/\mathrm{SC_{MODIS}}$) term, which accounts for the difference in solar irradiance between the two sensors.

The $\mathrm{Rad_{GEO}}$ values from *Aqua* MODIS and *GOES-13* pairings are linearly regressed through the C_0 of 29. In this study, this regression is referred to as the force fit. Obvious outliers, likely due to bad scan lines, are removed by excluding any pairings beyond 4 times the linear regression standard error (SE). Both the force fit (red line) and the linear regression with varying offset (black line) are shown in Fig. 1a. The linear regression more closely follows the ray-matched pairs and thus suggests a space count of 37.2, which is greater than the true space count of 29. Ignatov et al. (2005) states that the linear regression through the maintained space count provides a more accurate calibration than obtaining both the gain and the offset simultaneously. In other words, the *gain* and C_0 of the force fit and the linear regression should be equal under perfect conditions. Consistency between the two regression methods can validate the accuracy of the ray-matching algorithm. This case suggests that the CERES Edition 3 ray-matching algorithm needs further improvement.

It is assumed that the GEO visible imager calibration degrades gradually over time. A second-order trend

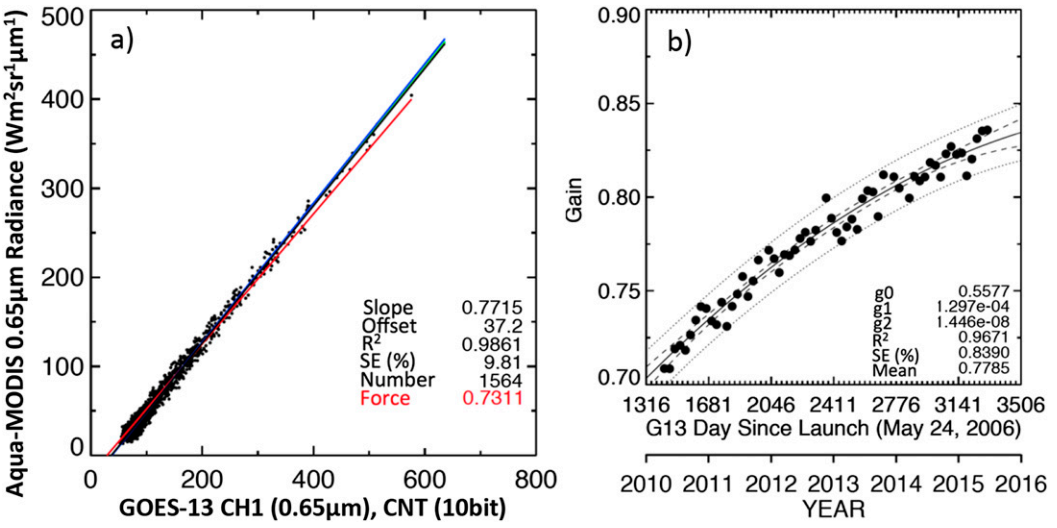

FIG. 1. (a) The CERES Edition 3 algorithm ATO *Aqua* MODIS and *GOES-13* ray-matched pairs with linear regression (black line) and force fit linear regression (red line) for April 2011. (b) The monthly *GOES-13* force fit gains, quadratic temporal trend (solid line), 95% prediction (dashed line), and confidence interval (dotted line). The associated temporal statistics are shown in the lower-right corner, where the *Mean* is the average of the monthly force fit gains over the timeline.

from the force fit monthly gains is calculated to provide quadratic gain coefficients (g_0, g_1, g_2) as a function of days since launch (dsl),

$$\text{gain} = g_0 + g_1\text{dsl} + g_2\text{dsl}^2. \quad (6)$$

Figure 1b shows the corresponding *Aqua* MODIS/*GOES-13* monthly force fit gains and the associated temporal quadratic regression designed to capture the temporal degradation of the sensor. The associated timeline SE about the regression is 0.84%, which is considered the temporal uncertainty of the ray-matched gain. A threshold of 50 monthly GEO/MODIS matches is specified to ensure only robust monthly force fit gains are used in the timeline.

The intercalibration of satellite sensors presents a matching challenge, which includes time, latitude, longitude, parallax, SZA, VZA, RAA, and wavelength (Wielicki et al. 2008). Three MODIS and GEO ray-matching improvements are considered: 1) the graduated angle method, which addresses the angular matching criteria; 2) the spectral band adjustment, which accounts for wavelength differences; and 3) a homogeneity filter, which addresses temporal/spatial discrepancies.

c. GAM

Figure 1a reveals significant scatter about the regression line. This scatter is due to the loosely constrained VZA and RAA matching criteria, which are designed to sufficiently sample bright clouds over all months of the year with the intent to avoid seasonal gain variations. Clear-sky scenes (low radiance) are anisotropic and require more restrictive angle matching, whereas optically thick clouds (high radiance) are nearly isotropic and allow for greater angle matching tolerance. Therefore, a graduated angle matching (GAM) methodology is employed that accounts for the fact that most matching pairs are observed over clear-sky conditions and for which a more restrictive angle criterion matching is required. In this use, graduated angle matching refers to a gradual change in allowance for angular difference. The *Aqua* MODIS radiance value is used to determine the angular matching tolerance. Between 0 and 100 $\text{W m}^{-2}\,\text{sr}^{-1}\,\mu\text{m}^{-1}$, and between 100 and 200 $\text{W m}^{-2}\,\text{sr}^{-1}\,\mu\text{m}^{-1}$, the VZA and RAA are matched within 5° and 10°, respectively. Otherwise, the VZA and RAA matching criteria remain unchanged at 15°. This strategy preserves all of the bright cloud ray-matched pairs but tightens the angular restrictions for dark scenes. Figure 2a reveals that the force and linear fits are more consistent after applying GAM, and that the linear regression offset of 34.3 is closer to the actual space count of 29 as compared with Fig. 1a. GAM eliminated nearly 80% of all matching pairs while also preserving the dynamic range and reducing the regression SE by 45%.

GAM was applied across five contemporary GEO sensors to test its effectiveness. Table 1 lists the five GEO satellites used in this study, along with their

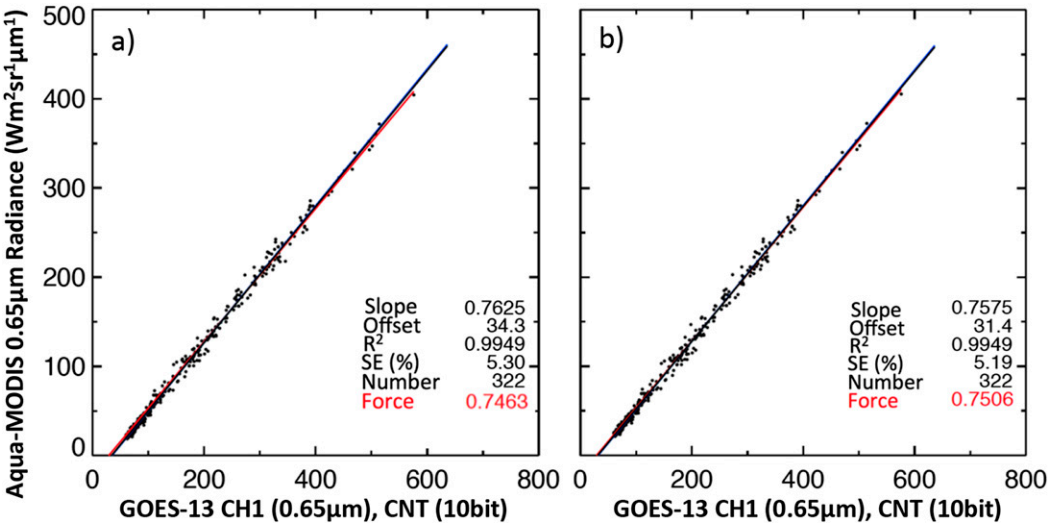

FIG. 2. (a) The CERES Edition 3 algorithm with GAM-applied ATO *Aqua* MODIS and *GOES-13* ray-matched pairs for April 2011. (b) As in (a), but with GAM and SBAF applied.

beginning and end record dates and subsatellite locations. Tables 2 and 3 contain the GEO/MODIS ray-matching statistics for the five GEO imagers. The number of matching pairs are reduced by ~70% (see Table 2, cf. Ed3 + GAM to Ed3), and the timeline mean monthly SEs are reduced by ~30% compared to Edition 3. The increased mean timeline *Aqua* MODIS radiance verifies that the restrictive angle matching mostly removed matched pairs over clear-sky conditions. The GAM approach reduces the timeline SE (especially for *GOES-15*), thus indicating that applying GAM mitigates the seasonal force fit gain noise. The gain differences between the linear and force fits and the difference between the regression offset and the space count are also reduced, except in the case of *MTSAT-2* (Table 3). Clearly, GAM has improved ray-matching precision.

d. ATO SBAF

For most GEOs, the visible-channel spectral bands are much broader than the corresponding *Aqua* MODIS band 1 as shown in Fig. 3. The nonoverlapping spectra must be accounted for to properly transfer the MODIS calibration to the GEO sensor. Chander et al. (2013) demonstrate that failure to correct for spectral band differences can result in significant calibration discrepancies. Properly accounting for the spectral band differences, whether owed to varying surface, aerosol, cloud, and/or atmospheric conditions, should make the ray-matched force fit and linear regressions more consistent.

Accurate spectral band normalization is challenging without the use of hyperspectral sensor radiances or radiative transfer models. Several studies have used ray-matched Global Ozone Monitoring Experiment (GOME) or SCIAMACHY hyperspectral radiances with LEO (Koelemeijer et al. 1998; Acarreta and Stammes 2005; Jourdan et al. 2007) and GEO imagers (Wu et al. 2011; Doelling et al. 2013c). Traditionally, radiative transfer models have been used to predict the at-sensor radiance based on surface spectral reflectivity and atmospheric conditions (Slater et al. 1987; Nagaraja Rao et al. 2001; Teillet et al. 2001; Henry et al. 2013). Recently, MODIS-based coincident cloud properties were used to predict the GEO sensor radiance for bright clouds (Ham and Sohn 2010; Okuyama 2011; Kim et al. 2014). A breakthrough, however, was reached when tropical land- and ocean-based a priori SBAFs derived from SCIAMACHY hyperspectral radiances were able to predict a MODIS/*GOES-12* ray-matched calibration gain within 0.3% (Doelling et al. 2012). The success of the SBAFs is owed to the fact that 10 years of continuous SCIAMACHY footprint observations are able to capture the variety of surface, cloud, and atmospheric conditions observed over ray-matching domains.

The SBAF algorithm (Doelling et al. 2011; Morstad et al. 2011; Scarino et al. 2012, 2016) employs the convolution of the SCIAMACHY nadir hyperspectral radiances with the target/reference sensor SRFs in order

TABLE 1. List of GEO satellites used in this study, their record beginning and end months, and the subsatellite longitudes.

GEO	Begin month	End month	Lon
GOES-15	Jan 2012	Jun 2015	135°W
GOES-13	May 2010	Jun 2015	75°W
Meteosat-9	May 2007	Dec 2012	0°
Meteosat-7	Feb 2007	Jun 2015	57°E
MTSAT-2	Jul 2010	Jun 2015	145°E

TABLE 2. The monthly *Aqua* MODIS and GEO ray-matched pair force fit statistics averaged over the GEO timeline, based on algorithm version. Ed3 represents the CERES Edition 3 algorithm and Ed4 is the CERES Edition 4 algorithm, which is the same as Edition 3 with the GAM, SBAF, and HF applied.

Satellite		*GOES-13*	*GOES-15*	*Meteosat-7*	*Meteosat-9*	*MTSAT-2*
Number of matched pairs	Ed3	2006	1252	1521	699	669
	Ed3+GAM	490	274	337	189	196
	Ed3+GAM+SBAF	493	275	335	189	193
	Ed4	404	198	256	162	158
Monthly SE (%)	Ed3	8.6	8.6	8.3	5.4	9.4
	Ed3+GAM	5.4	6.0	6.0	4.0	6.6
	Ed3+GAM+SBAF	5.3	5.9	5.8	3.8	6.6
	Ed4	5.0	5.2	5.3	3.7	5.9
MODIS Radiance ($\mathrm{Wm^{-2}\,sr^{-1}\,\mu m^{-1}}$)	Ed3	77.1	64.2	61.1	90.0	89.8
	Ed3+GAM	133.4	124.5	123.8	147.5	181.9
	Ed3+GAM+SBAF	134.4	126.0	123.7	149.3	180.3
	Ed4	146.7	149.3	146.1	160.0	206.5
Timeline SE (%)	Ed3	0.84	1.18	0.80	0.91	1.06
	Ed3+GAM	0.80	0.60	0.70	0.71	0.90
	Ed3+GAM+SBAF	0.79	0.73	0.72	0.67	0.85
	Ed4	0.78	0.72	0.74	0.67	0.93

to derive the sensor pseudoradiance values using Eq. (3) (substituting E_λ with SCIAMACHY hyperspectral radiances). The SBAFs used in this study were obtained from the website established by Scarino et al. (2016) (http://cloudsgate2.larc.nasa.gov/SBAF). MODIS and GEO pseudoradiance pairs are computed from all SCIAMACHY footprints contained in each ATO GEO domain during 2002 through 2010. The SBAF calculations obtained from the web tool used SCIAMACHY level-1b version-7.03 radiances (Skupin et al. 2005).

To guarantee the most accurate SBAFs, several orders of polynomial regression are applied to the GEO/MODIS pseudoradiance pairs until the SE of the regression is no longer significantly reduced. Table 4 displays the ATO SBAF results for *Aqua* MODIS band 1 for each of the five GEO imagers in Table 1. *Meteosat-7* exhibits the largest SE, which corresponds to having the largest bandwidth. On the other hand, *Meteosat-9*, which has an SRF very similar to that of MODIS, exhibits the smallest SE. The SE decreases significantly from using the force fit to the linear SBAF regression fit. The SE is slightly reduced between the linear and second-order fits. However, after applying a third-order fit, no further (significant) improvement in the SE is observed. Therefore, the *Aqua* MODIS and GEO pseudoradiance pairs are regressed using a second-order polynomial fit.

Figure 4a displays the SBAF results for *GOES-13*. Utilizing a second-order regression allows the SBAF to accommodate nonlinear radiance dependencies. Dark, clear-sky radiances will have an SBAF that differs from bright cloud radiances. A second-order SCIAMACHY-based SBAF with coefficients (a_0, a_1, a_2) captures accurately this radiance magnitude dependence, and is applied as follows:

$$\mathrm{Rad_{GEO}} = (a_0 + a_1\mathrm{Rad_{MODIS}} + a_2\mathrm{Rad^2_{MODIS}})(\mu_{0\mathrm{GEO}}/\mu_{0\mathrm{MODIS}}). \quad (7)$$

TABLE 3. As in Table 2, but showing gain and offset statistics. The GAM, SBAF, and HF force fit gain difference is the Ed3 to Ed3 + GAM, Ed3 + GAM to Ed3 + GAM+SBAF, and the Ed3 + GAM+SBAF to Ed4 gain difference, respectively.

Satellite		*GOES-13*	*GOES-15*	*Meteosat-7*	*Meteosat-9*	*MTSAT-2*
regression offset − space count	Ed3	6.4	4.6	1.2	2.7	−2.6
	Ed3 + GAM	4.1	4.4	1.1	2.8	−4.3
	Ed3 + GAM+SBAF	1.5	1.4	−0.1	1.1	−0.9
	Ed4	1.4	1.1	0.0	1.1	−0.3
Linear − force fit gain (%)	Ed3	4.2	3.0	2.0	1.0	−0.6
	Ed3 + GAM	1.6	1.7	1.1	0.5	−1.3
	Ed3 + GAM+SBAF	0.4	0.4	−0.5	0.5	−0.5
	Ed4	0.3	0.0	−0.4	0.2	−0.4
Force fit gain difference (%)	GAM	+1.6	+1.6	+1.0	+0.5	+0.4
	SBAF	+0.4	+0.5	−0.8	−1.8	−0.9
	HF	0.0	+0.3	0.0	+0.2	0.0

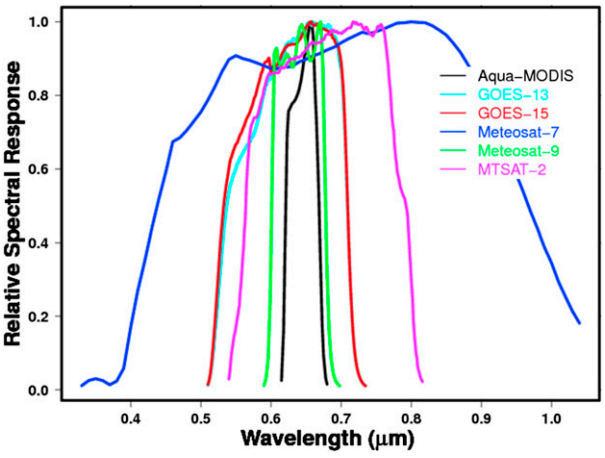

FIG. 3. The SRFs for *Aqua* MODIS, *GOES-13*, *GOES-15*, *Meteosat-7*, *Meteosat-9*, and *MTSAT-2* band 1 visible channels.

e. DCC SBAF

The *approximate DCC* dataset compiled within the Scarino et al. (2016) website is used to compute the DCC SBAF. Similar to the ATO SBAF, the GEO and MODIS DCC pseudoradiance pairs are regressed through several polynomial orders in order to find the fit with the lowest SE (Table 4). No significant SE reduction is observed beyond the force fit. The *GOES-13* and MODIS DCC pseudoradiances are very linear in nature as illustrated by Fig. 4b. This linearity, which can be described by a single factor obtained from the force fit, is what makes interband calibration based on DCC, as used by other studies, possible (Vermote and Kaufman 1995; Le Marshall et al. 1999; Lafrance et al. 2002; Fougnie and Bach 2009). As predicted, the DCC SBAF has a much lower SE than that of the ATO SBAF (Table 4), which lends merit to studying the feasibility DCC GEO/MODIS ray matching. The force fit SCIAMACHY-based SBAF with coefficient f_1 is used to compute the MODIS-predicted ray-matched $\mathrm{Rad_{GEO}}$ as follows:

$$\mathrm{Rad_{GEO}} = f_1(\mathrm{Rad_{MODIS}})(\mu_{0\mathrm{GEO}}/\mu_{0\mathrm{MODIS}}). \quad (8)$$

The ATO and the DCC SBAF should eventually become similar for large radiance values. Therefore, in order to ensure convergence of the DCC and ATO fit for radiances greater than 400 $\mathrm{W\,m^{-2}\,sr^{-1}\,\mu m^{-1}}$, the DCC SBAF replaces the ATO SBAF.

Figure 2b displays the *GOES-13* count and *Aqua* MODIS radiance ray-matched pairs for April 2011 using both GAM and SBAF. Compared to Ed3 + GAM, adding the SBAF has reduced the space count by ~3 (closer to the maintained space count of 29) and the difference between the force and linear fits is from 2.1% to 0.9%. The SBAF may improve the regression SE because it can resolve nonlinearities. Table 2, however, indicates that the SBAF did not significantly change either the monthly or timeline SE. Table 3, on the other hand, shows that the regression offset and space counts, and the linear and force fit gains are much more consistent after applying SBAF. This consistency indicates that the SBAF is more accurate than the SC ratio.

f. HF

To match the GEO and MODIS pixel field-of-view (FOV) differences and to reduce the impact of navigation/pointing errors, parallax errors, and advection-induced mismatched radiation fields, a large 0.5° latitude × 0.5° longitude intercalibration footprint (ICF) is used for CERES Edition 3 processing (Minnis et al. 2002). CERES processing also employs subsampled GEO visible at the IR nominal pixel resolution and subsampled MODIS visible at 2 km, thus requiring a larger ICF than using nominal pixel resolution data. Increasing the size of the ICF reduces the spatial matching noise, but it also reduces the number of independent matched pairs and the extent of the dynamic range. Also, using a larger ICF is more effective in mitigating ray-matching noise than reducing the time difference (Wielicki et al. 2008).

Another way to reduce the spatial matching noise without increasing the ICF size is to use a spatial uniformity or homogeneity filter (HF). The HF reduces the monthly force fit SE by removing outliers (Doelling

TABLE 4. The *Aqua* MODIS band 1 and GEO visible-channel SCIAMACHY footprint pseudoradiance pair regression SEs (%) for the GEO ATO and DCC domains as a function of the SBAF regression order.

Satellite		*GOES-13*	*GOES-15*	*Meteosat-7*	*Meteosat-9*	*MTSAT-2*
ATO	Force	1.99	2.16	4.09	0.59	1.85
	Linear	1.04	1.10	2.54	0.31	1.52
	2nd	0.98	1.03	2.23	0.30	1.35
	3rd	0.98	1.02	2.22	0.29	1.35
DCC	Force	0.372	0.386	1.58	0.138	0.380
	Linear	0.370	0.384	1.58	0.134	0.374
	2nd	0.368	0.382	1.57	0.137	0.374

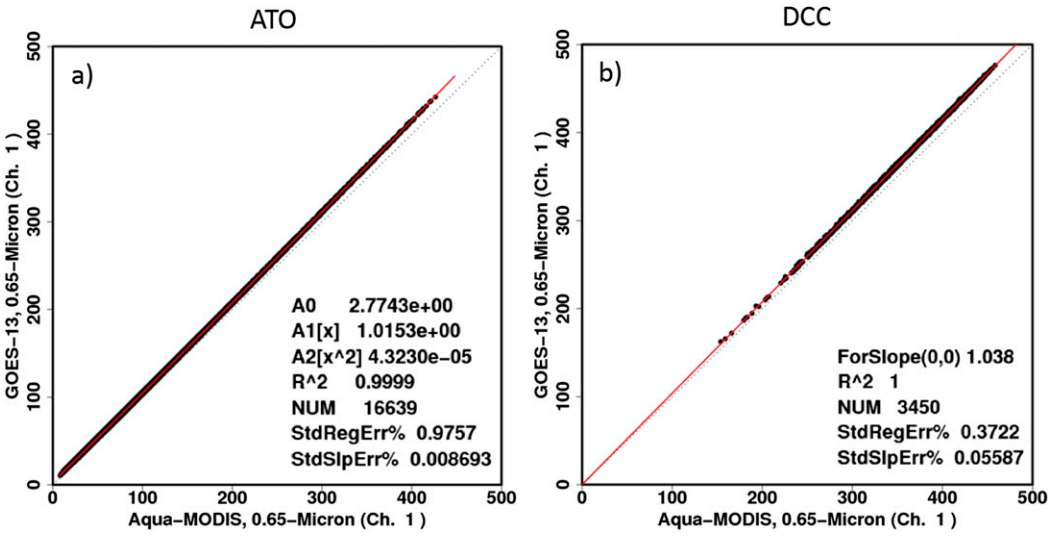

FIG. 4. The *Aqua* MODIS band 1 and *GOES-13* visible-channel SCIAMACHY footprint pseudoradiance pairs for the (a) *GOES-13* ATO domain overlaid with a second-order fit and (b) DCC footprints with a force fit.

et al. 2011). However, setting an aggressive HF limits the sampling to mostly clear-sky conditions. This level of filtering may cause the dynamic range to vary with season depending on the bright cloud amount in the GEO domain, which contributes to the seasonal noise about the timeline trend.

The ray-matched force fit sensitivities, using GAM, SBAF, and HF, are plotted in Fig. 5 for the five GEO satellites. The HF is defined as the pixel radiance standard deviation divided by the mean within the ICF, and is varied to determine the impact on the regression statistics. Figures 5a and 5b show that the number of monthly pairs and the monthly force fit SEs are significantly reduced if the HF is set below 0.7. If the HF is set below 0.5, then the number of viable months, which must have at least 50 matched pairs, is dramatically reduced (Fig. 5c). Ideally, the HF will reduce the monthly gain variability over the timeline without excessively sacrificing dynamic range and sample size. Figure 5d shows no change in the timeline SE for an HF greater than 0.7, and it shows inconsistent SE for HF less than 0.7, the latter of which is due to the reduction of viable monthly gains. An HF of 0.7 is chosen, which balances the monthly force fit SE with the timeline SE.

Figure 6a highlights the effect of applying HF to the GAM and SBAF ray-matched algorithm. By including HF, the monthly force fit SE was reduced from 5.2% (Fig. 2b) to 4.7% while removing ~20% of the pairs, thereby indicating that the HF was effective in removing outliers while maintaining the extent of the dynamic range. Table 2 verifies that HF mostly removed clear-sky pairs, given that the mean timeline *Aqua* MODIS radiance increased with ~20% of matched pairs removed (cf. Ed3 + GAM + SBAF to Ed4). As expected, the HF slightly decreased the monthly SE while not affecting the timeline SE, except for *MTSAT-2*. The regression

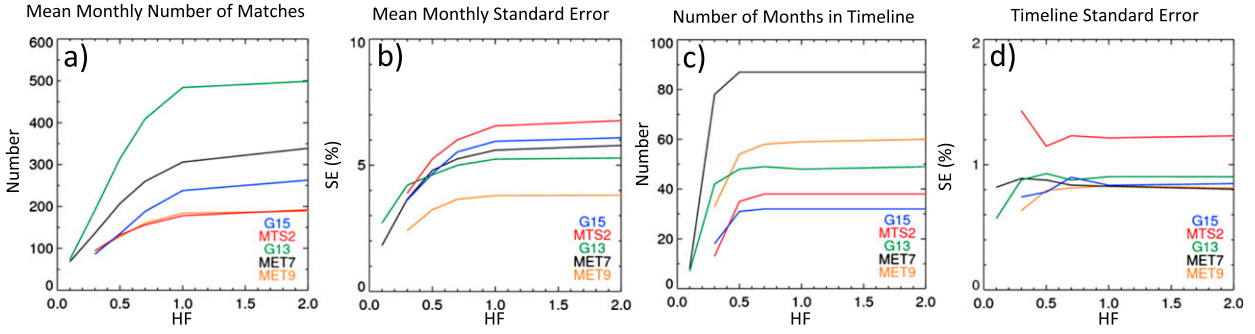

FIG. 5. (a) The mean number of monthly ray-matched pairs. (b) The mean monthly force fit gain SE for the given GEO and *Aqua* MODIS pair over the timeline as a function of HF. (c) The number of monthly gains used in the trend and (d) the associated trend SEs are also shown.

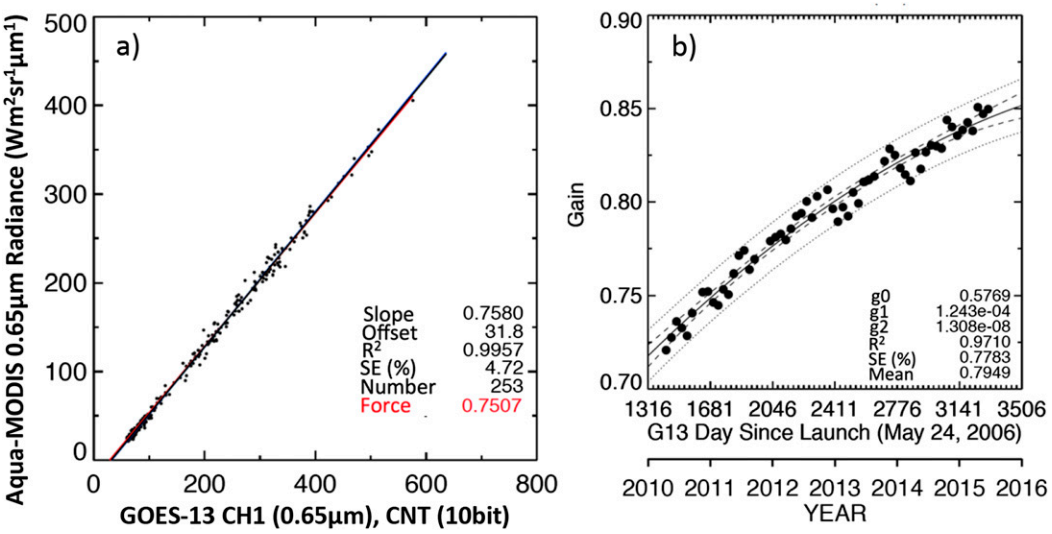

FIG. 6. (a) The CERES Edition 4 algorithm (includes GAM, SBAF, and HF) ATO *Aqua* MODIS and *GOES-13* ray-matched pairs. (b) The monthly *GOES-13* force fit gains for April 2011.

offset-minus-space-count difference as well as the linear-minus-force fit-gain difference were also slightly reduced (Table 4).

g. Edition 4

The CERES Edition 4 GEO ray-matching algorithm constitutes the additions of GAM, the SBAF, and HF to the baseline Edition 3 approach. Although all three additions offer improvement, Table 3 clearly shows that the SBAF had the greatest impact on ensuring offset consistency. The Edition 4 ray-matching approach reduces the gain difference to within 0.4%, indicating that these improvements mitigate angular and spectral matching biases. The individual GAM, SBAF, and HF improvements have changed the value of the force fit gains by up to 1.8%. The individual GAM and SBAF components can alter the force fit gains in the same direction, as is the case with *GOES-13*, and *GOES-15*, or have compensating biases for the remaining GEOs. To obtain ray-matched calibration accuracies better than 1%, the spectral band differences must be accounted for, and the angle matching tolerances must be as restrictive as allowable.

3. DCC ray matching

a. Methodology

The objective of the DCC ray-matching algorithm is to locate DCC cores within a MODIS swath over the relevant GEO domain where GEO and MODIS angles match. The coincident GEO and MODIS pixel-level measurements within the same areal extent, defined by the convective core boundary, are averaged, and then regressed monthly similar to the ATO ray-matching algorithm. The monthly computed gains are then monitored over time to compute calibration gain coefficients.

The MODIS imagery is used to locate the convective cores. All daytime *Aqua* MODIS 5-min granules that cross the equator between ±40° in longitude about the GEO subsatellite location, and within ±20° latitude, are listed. Initially the DCC identification criteria are broadly defined in order to construct the DCC dataset, and then they are further refined with subsequent processing. All MODIS pixels within a granule having VZA $<$ 40°, and an 11-μm brightness temperature (BT) $<$ 220 K, are identified as potential DCC core centers. The corresponding GEO SZA, VZA, and RAA are computed from the latitude, longitude, and time of the MODIS pixel and GEO subsatellite location. If the MODIS and GEO VZA (RAA) differences are less than 15° (25°), then a potential ray-matched DCC pixel is identified. Unfortunately, DCC core diameters vary greatly, and thus developing automated software to identify these centers is challenging (Berendes et al. 2008; Hennon et al. 2011). Therefore, two DCC core diameters, or ICFs, are predefined at 10 and 30 km. This study incorporates the *Aqua* MODIS C6 2-km subsampled pixels, that is, skipping every other 1-km pixel in both the orbit and scan direction. For the 10-km ICF, the average radiance is computed from the 5 × 5 MODIS pixels centered at the DCC location for both the MODIS band 1 (0.65 μm) and band 31 (11 μm) channels (see Table 5). The standard deviation is computed from a field of 7 × 7 pixels. For the 30-km ICF, the

TABLE 5. The *Aqua* MODIS and GEO pixel spacing and line × element field used to define the DCC 10-km ICF and 30-km ICF.

Satellite line×pixel (km)	Pixel spacing	10-km ICF		30-km ICF	
		Mean	Std dev	Mean	Std dev
MODIS	2×2	5×5	7×7	15×15	17×17
GOES-13/15	1×0.58	9×15	13×23	29×51	33×57
Meteosat-9	3×3	3×3	5×5	11×11	13×13
Meteosat-7	2.5×2.5	5×5	7×7	13×13	15×15
MTSAT-2	1×1	9×9	13×13	29×29	31×31

radiance mean is from a 15 × 15 pixel field, and the standard deviation is from a 17 × 17 field centered at the identified DCC pixel.

Because the MODIS pixel spacing is 2 km, there can be many overlapping DCC ICFs. Therefore, overlapping DCC ICFs are eliminated before analysis. The identified DCC ICFs are sorted by BT. The coldest ICF is selected first and then all of the remaining ICFs that overlap with the selected ICF are eliminated from the sorted list. This procedure is repeated for the image until no additional ICF can be removed from the sorted list. Figure 7 displays an *MTSAT-2* visible image with the nonoverlapping DCC ICFs overlaid. None of the ICFs intersect, thereby validating the procedure.

The GEO data are obtained from the University of Wisconsin via the McIDAS software (Lazzara et al. 1999). GEO image scanning operates on a daily schedule. For each image scanned during the day, the scan time at the equator is saved. The GEO image with the closest time to the MODIS DCC ICF is used to find the corresponding GEO DCC ICF radiance. McIDAS navigation software is used to locate the 1-km nominal GEO visible image line and element based on the MODIS DCC center pixel latitude and longitude, as well as to compute the GEO SZA, VZA, and RAA. An odd number of pixels in both the line and element directions from the DCC center pixel is used to construct the GEO ICF based on the GEO nominal pixel spacing that matches the MODIS ICF. The GEO nominal pixel spacing and GEO ICF pixel field are shown in Table 5. The mean and standard deviation of the visible-channel counts are computed for both the 10- and 30-km DCC ICFs. The DCC ray-matched MODIS and GEO ICF radiance pairs are then regressed to compute the monthly gain, similar to the ATO ray-matching algorithm. The DCC SBAF is applied to the MODIS radiance using Eq. (8) before

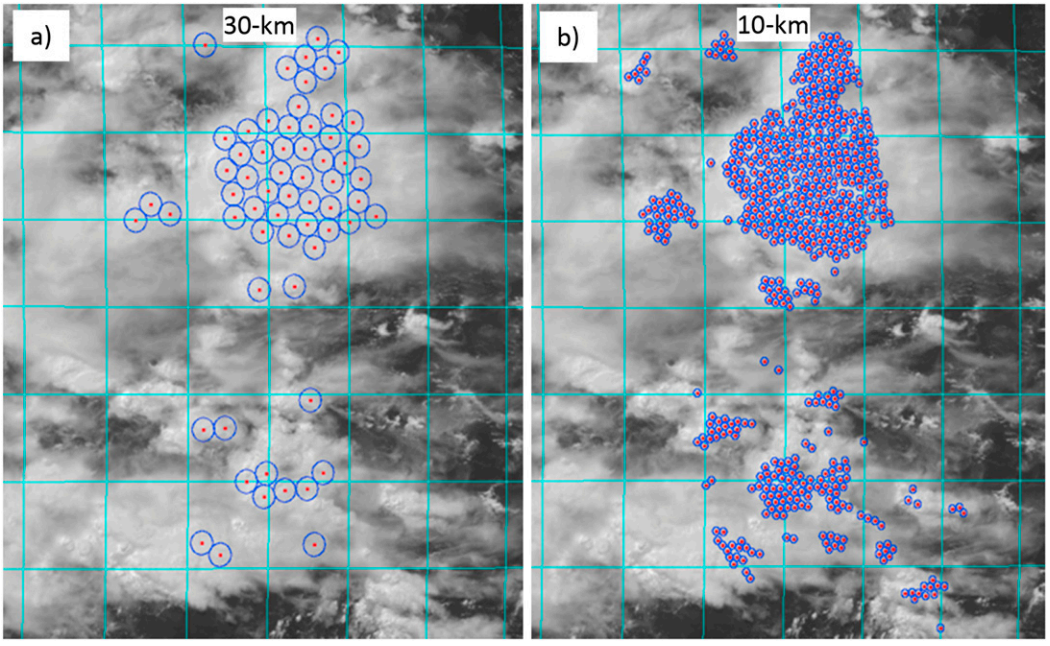

FIG. 7. The (a) 30- and (b) 10-km *Aqua* MODIS and *MTSAT-2* ray-matched DCC ICF pairs overlaid on the *MTSAT-2* 1-km visible image for 0432 UTC 20 Jul 2011. The cyan squares delineate the 1° × 1° latitude by longitude grid. The red points represent the center of the ICF, and the blue circles represent the boundary of the ICF.

TABLE 6. The DCC ray-matching statistics as a function of criteria and threshold for the DCC 10- and 30-km ICF. The terms $N_{Monthly}$ and $SE_{Monthly}$ denote the monthly mean number of ray-matched pairs and force fit SEs, respectively, over the *MTSAT-2* timeline. The term SE_{Trend} is the quadratic trend SE from the monthly force fit gains. The baseline dataset uses a 220-K MODIS BT threshold, and the scattering angle and time differences must be within 15° and 15 min, respectively, between GEO and MODIS. The baseline dataset does not utilize any visible or BT HFs, VZA, or SZA constraints.

Parameter	Threshold 10 km/30 km	DCC 10-km ICF			DCC 30-km ICF		
		$N_{Monthly}$	$SE_{Monthly}$	SE_{Trend}	$N_{Monthly}$	$SE_{Monthly}$	SE_{Trend}
Baseline dataset	None	23 065	6.1	0.44	2230	3.8	0.44
Visible HF (%)	<0.1/0.2	16 521	3.8	0.49	2037	3.1	0.48
	<0.05/0.1	8666	2.8	0.54	1178	2.4	0.58
	<0.025/0.05	2311	2.1	0.70	391	1.9	0.66
BT HF (K)	<4.0/7.5	15 955	4.7	0.47	1844	3.3	0.49
	<2.0/5.0	6835	3.9	0.56	1292	3.0	0.53
	<1.0/2.5	1235	3.4	0.85	342	2.6	0.76
BT threshold (K)	<210	9363	5.2	0.56	878	3.3	0.53
	<205	4583	4.7	0.74	404	3.0	0.71
	<200	1706	4.3	1.13	137	2.7	1.05
Time diff (min)	<10	18 247	5.6	0.52	1822	3.6	0.56
	<5	9303	5.3	0.59	915	3.3	0.59
	<2.5	4765	5.3	0.71	470	3.3	0.74
Scattering angle (°)	<10	6353	5.4	0.54	612	3.1	0.51
	<5	2536	5.0	0.62	248	2.9	0.63
SZA (°), VZA(°)	<40, <40	12 854	5.9	0.50	1299	3.4	0.42
	<30, <30	3806	5.6	0.64	394	3.1	0.51

regression analysis in order to mitigate biases induced by spectral band differences.

b. *Threshold sensitivity analysis*

The DCC identification and GEO/MODIS matching criteria can now be optimized to minimize the monthly force fit SE and the timeline SE. Tightening the matching thresholds should decrease the monthly force fit SE. If the sampling is insufficient, then the noise in the monthly force fit gains and the associated timeline SE will increase. To ensure robust sampling for all dates in the timeline, the months with the fewest DCC are used to determine the threshold magnitude needed to derive the smallest timeline SE. Both the temporal and angular difference-matching criteria are evaluated. Reducing the time difference decreases the DCC core spatial displacement between GEO and MODIS images due to advection. Reducing the angular difference decreases the DCC GEO and MODIS bidirectional reflectance distribution function (BRDF) biases. The BRDF-induced biases may introduce a seasonal oscillation in the timeline monthly gains because the DCC are in phase with the area of direct solar heating within the intertropical convergence zone (ITCZ). The more isotropic part of the DCC BRDF is where the SZA and VZA are closest to the zenith. Reducing the SZA and VZA should decrease the BRDF biases that are caused by the GEO and MODIS angle matching differences. To ensure identification of the DCC core rather than the edge, HF in the visible and IR, as well as colder BT thresholds, are used (Doelling et al. 2013b). MODIS and GEO navigation, time matching, parallax, and three-dimensional differences are mitigated if the ICF is located over the homogenous DCC core rather than over the DCC edge.

The *MTSAT-2* record is used to test the sensitivity of the DCC identification criteria and the MODIS/GEO matching thresholds. Table 6 displays the monthly mean number of GEO and MODIS pairs, force fit SE, and the timeline SE for both the 10- and 30-km ICFs. The Table 6 *baseline dataset* applies a 220-K BT threshold, and the GEO–MODIS scattering angle and time difference must be within 15° and 15 min, respectively. The baseline dataset does not utilize visible or IR HFs, nor VZA or SZA constraints. The baseline dataset is used to compare the individual threshold sensitivities. In general, the tightening of the thresholds decreases the monthly regression SE while significantly reducing the number of monthly GEO and MODIS radiance pairs (Table 6). The visible HF is most effective in reducing the monthly regression SE, whereas the IR HF and BT thresholds are somewhat effective. The time difference, scattering angle, SZA, and VZA thresholds are the least effective in reducing monthly regression SE. For all parameters, the individual thresholds did not reduce, but rather increased the timeline SEs, with the exception of the VZA and SZA 40° thresholds for the 30-km ICF.

The second sensitivity tests were conducted for all five GEO satellites using a *baseline*, *broad,* and *narrow*

TABLE 7. The DCC 10- and 3-km ICF ray-matching baseline, broad, and narrow dataset HF thresholds. *All datasets* use a VZA and SZA threshold of 40°.

Dataset	Baseline		Broad		Narrow	
	10 km	30 km	10 km	30 km	10 km	30 km
Visible	None	None	0.1	0.2	0.05	0.1
BT (K)	None	None	4.0	7.5	2.0	5.0

combination of visible and IR HF datasets as listed in Table 7. Table 8 displays the monthly number of GEO and MODIS pairs, the force fit SE, and the gain averaged over the timeline. In general, the smallest timeline SE is exhibited in the *broad dataset*. The mean timeline gain typically decreases slightly for tighter thresholds, except for the *Meteosat-9* 30-km ICF. In general, the mean timeline gain difference between the baseline and broad datasets is greater than the broad and narrow datasets. This pattern indicates that further tightening of the thresholds will not change the overall mean timeline gains. The last column in Table 8 shows that the broad dataset 10- and 30-km ICF mean timeline gain ratios are within 0.15% for all GEOs, except for *Meteosat-9*. For *Meteosat-9*, the narrow dataset gain ratio is 0.09%. The consistency of the 10- and 30-km ICF mean timeline gain ratios validates the optimization of the thresholds to remove any potential angular matching biases.

4. DCC and ATO ray-matching comparisons

a. Monthly regressions

The DCC broad dataset 10- and 30-km ICF and the ATO Edition 4 (GAM, SBAF, and HF applied) *MTSAT-2*/MODIS ray-matched pairs are compared in Fig. 8. January and October 2013 are displayed to represent months with abundant and sparse sampling, respectively. The number of matched pairs is greatest for the DCC 10-km ICF technique and least for the ATO ray-matched method, whereas the regression SE is least for the DCC 10-km ICF and greatest for the ATO ray-matching method. For DCC, the ray-matched pairs are concentrated along the force fit regression, suggesting that the DCC ray-matching methodology is robust.

Figure 9a reveals that the DCC ray-matched monthly regression SEs are similar over time, unlike the ATO SEs. This fact verifies that the DCC ray-matching algorithm captures the same cloud conditions over the satellite record, whereas the ATO algorithm identifies a wide variety of cloud and surface (scene) conditions over time. Each scene type requires its own unique SBAF, which if not accurate will add noise to the monthly force fit gains. Figure 9b shows that the monthly mean *Aqua* MODIS radiances are remarkably stable over time, which is accomplished by accurately identifying DCC cores, and having sufficient DCC sampling, and is owed to the fact that MODIS calibration is stable over time. Figure 9c shows the corresponding monthly mean *MTSAT-2* count, which indicates a slight decrease over time, thereby implying that the *MTSAT-2* sensor is degrading.

b. Temporal trends

If both the DCC and ATO ray-matching algorithms were perfect, then the DCC and ATO force fit gains would be equivalent. Figure 10 displays the DCC 10- and 30-km ICF and the CERES Edition 4 ATO monthly

TABLE 8. The DCC ray-matching statistics as a function of baseline, broad, and narrow dataset (see Table 7) for the DCC 10- and 30-km ICF. The term N_{Monthly} denotes the monthly mean number of ray-matched pairs over the GEO timeline. The term SE_{Trend} is the quadratic trend SE from the monthly force fit gains, and *gain* represents the average of the monthly force fit gains over the GEO timeline.

Satellite	HF Threshold	DCC 10-km ICF			DCC 30-km ICF			Gain ratio 10 km/30 km
		N_{Monthly}	SE_{Trend}	Gain	N_{Monthly}	SE_{Trend}	Gain	
GOES-15	Baseline	3959	0.46	0.7788	407	0.37	0.7766	0.28
	Broad	2652	0.44	0.7775	338	0.36	0.7765	0.13
	Narrow	996	0.45	0.7773	151	0.50	0.7726	0.61
GOES-13	Baseline	7537	0.59	0.7910	706	0.51	0.7871	0.50
	Broad	3776	0.46	0.7863	460	0.42	0.7852	0.14
	Narrow	1258	0.55	0.7851	235	0.45	0.7844	0.09
Meteosat-9	Baseline	8514	0.45	0.5573	823	0.45	0.5535	0.69
	Broad	4927	0.41	0.5559	581	0.41	0.5544	0.27
	Narrow	2017	0.41	0.5557	336	0.43	0.5552	0.09
Meteosat-7	Baseline	4689	1.01	0.6215	465	0.74	0.6172	0.70
	Broad	2875	0.62	0.6144	357	0.67	0.6140	0.07
	Narrow	1173	0.71	0.6130	215	0.75	0.6132	0.03
MTSAT-2	Baseline	12 730	0.50	0.5952	1285	0.42	0.5926	0.44
	Broad	7382	0.46	0.5913	954	0.41	0.5910	0.05
	Narrow	1779	0.59	0.5908	366	0.52	0.5905	0.05

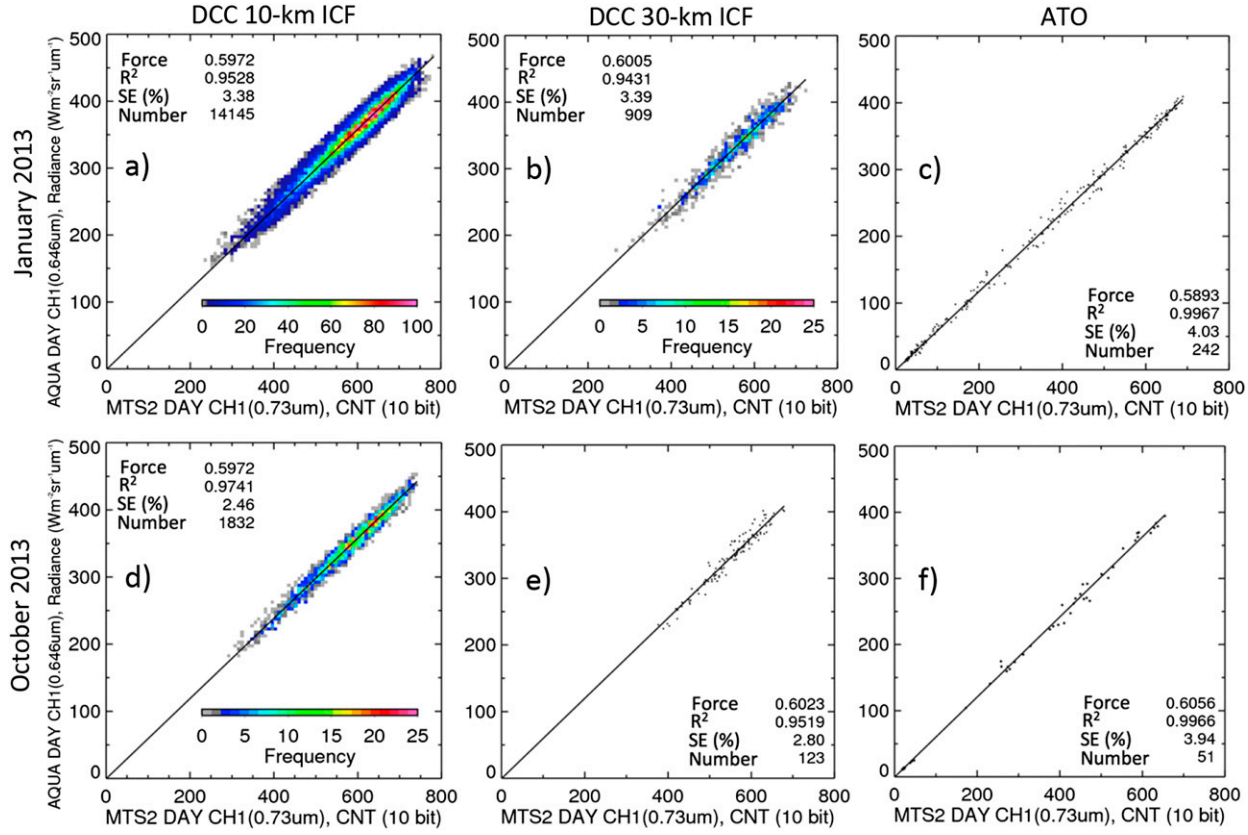

FIG. 8. The (a) DCC 10-km ICF, (b) DCC 30-km ICF, and (c) ATO *Aqua* MODIS/*MTSAT-2* ray-matched pairs and associated force fit and statistics for January 2013 using the DCC broad dataset. The (d) DCC 10-km ICF, (e) DCC 30-km ICF, and (f) ATO *Aqua* MODIS and *MTSAT-2* ray-matched pairs and associated force fit and statistics for October 2013.

force fit gains for the five GEOs. The DCC method used the broad dataset HF thresholds found in Table 7 for all GEOs. Qualitatively, the ATO monthly gains show greater scatter about the second-order temporal regression line compared to the DCC ray-matched gains. The DCC 10- and 30-km ICF ray-matched monthly force fit gains are very consistent, indicating that they are capturing the same DCC. All GEO DCC ray-matched monthly force fit gains show distinct seasonal cycles, especially for *Meteosat-9* and *Meteosat-7*.

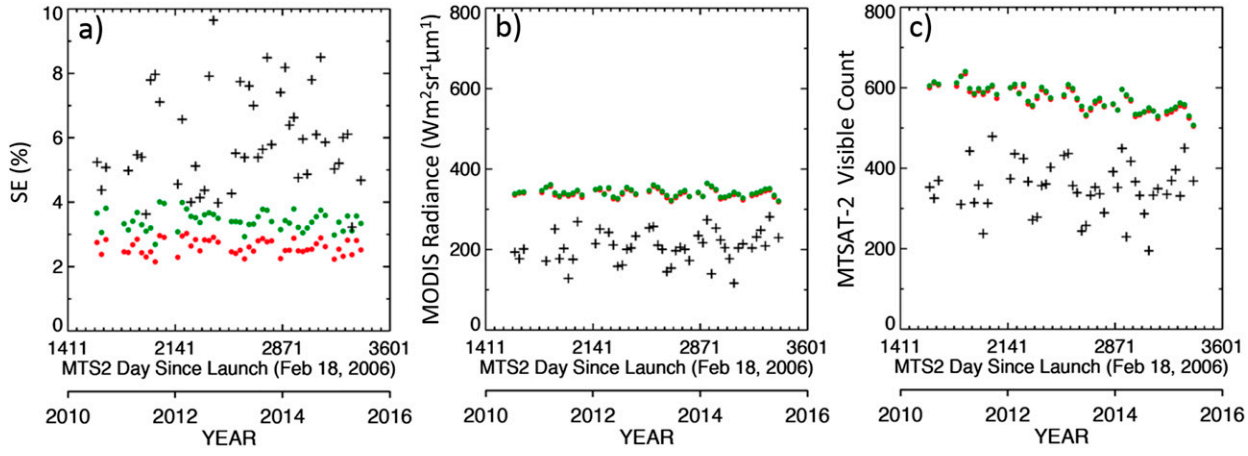

FIG. 9. The (a) monthly *Aqua* MODIS radiance and *MTSAT-2* ray-matched force fit SEs, (b) monthly mean *Aqua*-MODIS radiance, and (c) monthly mean *MTSAT-2* visible count for ATO (black +), DCC broad dataset 10-km ICF (green •), and DCC broad dataset 30-km ICF (red •).

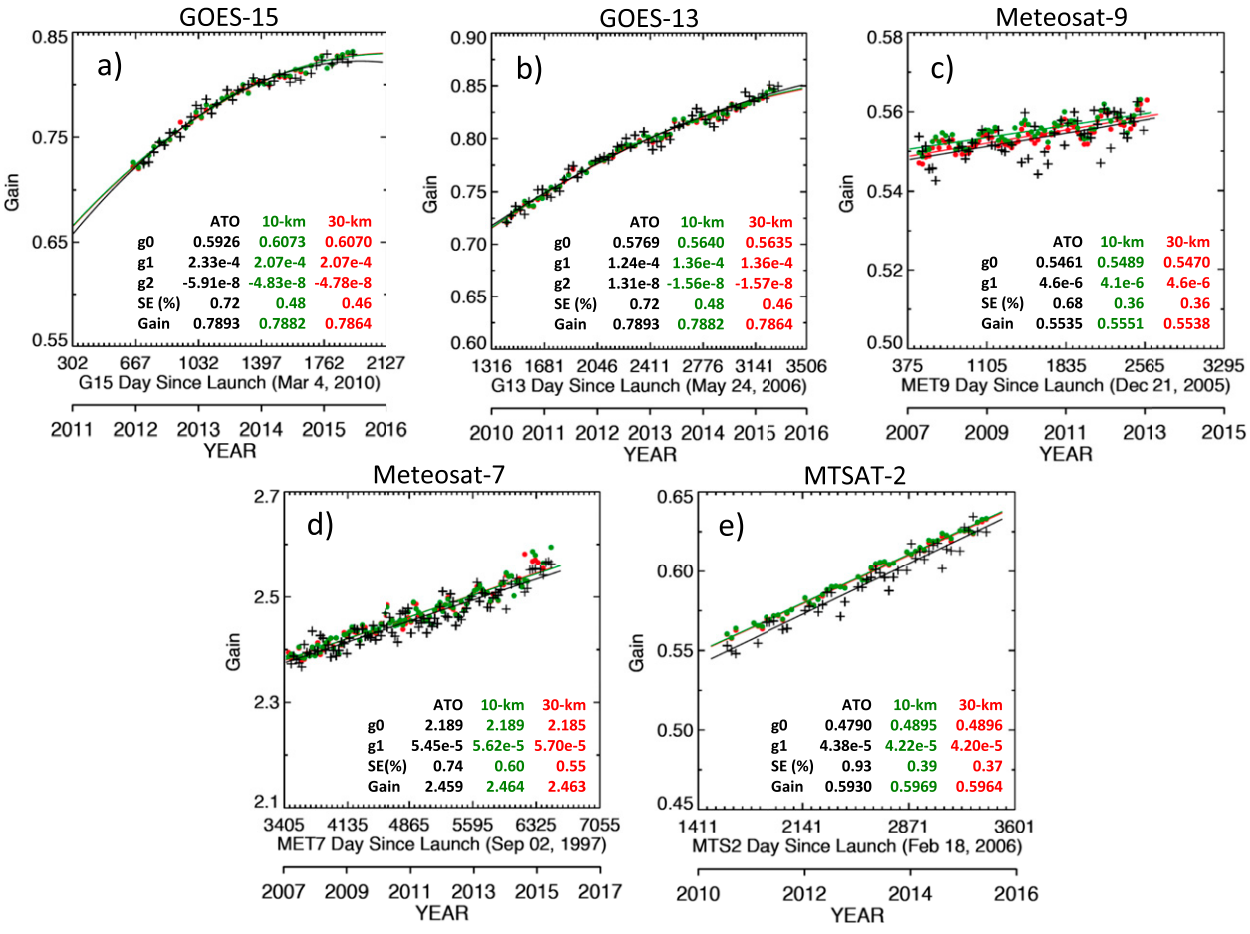

FIG. 10. The ATO (black +), DCC 10-km ICF (green •), and DCC 30-km ICF (red •) ray-matched monthly force fit gains, trend regression lines, and associated statistics, where the *gain* represents the average of the monthly force fit gains over the timeline, for (a) *GOES-15*, (b) *GOES-13*, (c) *Meteosat-9*, (d) *Meteosat-7*, and (e) *MTSAT-2*. All GEOs used the DCC broad dataset.

Quantitatively, the mean timeline gains for all ray-matched methods are within 0.4%, except for *MTSAT-2*, which is 0.65%. This self-consistency validates both ray-matching algorithms. The DCC 10- and 30-km ICF timeline gains are within 0.25%. The DCC ray-matching trend SEs are within 0.5%, except for *Meteosat-7*. Ray matching over DCC has reduced the GEO gain timeline SE by 20%–60% of what can be achieved from the ATO algorithm alone. This result is due to the fact that DCC have the smallest SBAF, are nearly isotropic, and have the greatest signal-to-noise ratio of all Earth scene types.

5. Conclusions

The CERES Edition 4 processing effort is underway, which has allowed the opportunity to recalibrate the GEO imager visible radiances, and thereby improve the cloud and radiation retrievals used to estimate TOA SW fluxes from the CERES *Terra* and *Aqua* MODIS measurements. CERES relies on ray matching to transfer the *Aqua* MODIS C6 band 1 calibration to the GEO imagers in order to derive consistent cloud properties and fluxes across the 16 GEOs in the CERES record.

Sensor ray matching requires precise time, spatial, angular, and spectral alignment. It is a delicate balance between sufficient sampling and precision. Matching criteria that are too tolerant may introduce biases and will increase the uncertainty of the gain. The use of precise matching criteria requires long time intervals in order to obtain sufficient sampling, thus making short-term sensor degradation monitoring difficult. The CERES Edition 3 GEO calibration angle matching criteria were too broad and only accounted for the difference in the solar incoming radiation in order to denote the spectral band difference. The CERES Edition 4 GEO calibration uses a graduated angle matching method designed to be more restrictive for anisotropic clear-sky ocean (dark) radiances and less restrictive for

isotropic bright clouds. Fortunately, the restrictive angular thresholds provided sufficient clear-sky sampling while maintaining Edition 3 bright cloud sampling. For Edition 4, the SBAF accounts for both the solar incoming and Earth reflected spectra in order to explain spectral band differences. The SBAF represents the average conditions over the ray-match domain and is a function of the radiance magnitude, that is, it is specific to the Earth-viewed scene. Large 0.5° ICF and the use of HF mitigate any remaining mismatching error owed to sensor navigation, parallax error, and/or advection-induced radiation field misalignment. These ATO ray-matching improvements were tested across five contemporary GEO imagers.

Successfully, minimizing the gain difference between the linear regression and the regression through the maintained GEO space count validates the ray-matching improvements. The resulting gain difference was reduced to within 0.4% by incorporating the GAM, SBAF, and HF improvements. Individually applying GAM, SBAF, and HF altered the resulting calibration gain by up to 1.8%, indicating that loosely constrained matching criteria, or inadequate SBAFs, not only increase the uncertainty of the derived gain but may also induce bias. To obtain ray-matched calibration accuracies better than 1%, the spectral band differences must be accounted for, and the angle matching tolerances must be as restrictive as possible

Deep convective clouds are the brightest isotropic Earth targets with near-uniform visible spectra, and thus are of the most suitable targets for ray-matching. A 10- and 30-km-core DCC ray-matching algorithm was presented, and their resulting mean timeline gains are within 0.25%. The mean timeline gains for both the ATO and DCC ray-matched methods are within 0.4% (except for *MTSAT-2* with 0.65%), thus validating both ray-matching methods. However, the DCC ray-matching timeline SEs are within 0.5% and represent a 20%–60% reduction from those of the ATO ray-matched algorithm. CERES Edition 4 utilizes the GEO ATO ray-match calibration gains, which will be validated with the DCC ray-matched gains, as well as desert and DCC invariant target calibration gains (Bhatt et al. 2014; Doelling et al. 2011). The CERES Edition 4 calibration gains should yield consistent GEO-derived fluxes and cloud properties from the CERES SYN1deg product, and will benefit the broader GEO retrieval community.

Acknowledgments. This work was supported by the National Aeronautics and Space Administration Earth Science Enterprise Office through the CERES and the Satellite Calibration Interconsistency programs (NNH11ZDA001N-ROSES-2011 A.29 Satellite Calibration Interconsistency Studies). The GEO satellite data were obtained from the University of Wisconsin Space Science and Engineering Center, Madison, Wisconsin. The authors thank the GSICS Research Working Group for the insightful discussions.

APPENDIX

GEO/MODIS Ray-Matched Spatial Sampling

The GEO/MODIS angular matching locations are sparse and systematic. Usually, the operational GEOs maintain a fixed scanning schedule and the *Aqua* or *Terra* satellite orbits are maintained with a short 16-day repeat cycle. Therefore, the locations generally repeat annually, and the daily locations change gradually according to the position of the sun. To demonstrate, *MTSAT-2*/*Aqua* MODIS ray-matched spatial sampling is highlighted in this appendix section. These ray-matched locations are easily predictable using the Keplerian orbital elements commonly found in the two-line element (TLE) format. Daily North American Air Defense Command (NORAD) TLEs, available on the Celestrak website, are used to locate the *Aqua* satellite. The Consultative Committee for Space Data Systems (CCSDS) 301.0-B-2 *Astronomical Almanac* ephemeris data are used to compute solar angles and are available in the SDP toolkit for the EOSDIS Core System Project (http://newsroom.gsfc.nasa.gov/sdptoolkit/toolkit.html).

To plot the viewing and solar conditions, a 0.5° latitude × 0.5° longitude grid is centered at the *MTSAT-2* subsatellite point positioned at 145°E, and is extended ±30° and ±45° in the latitude and longitude directions, respectively. At each grid center, the VZA, SZA, and RAA are computed for both *Aqua* MODIS and *MTSAT-2*. Figure A1 shows a 2 January 2013 example. The *Aqua* orbit is in the ascending node and is passing the equator at 0244 UTC. The *Aqua* orbit track is easily found at the VZA minima. The corresponding *MTSAT-2* VZAs were computed as if the image were scanned instantaneously at 0244 UTC, where concentric rings of equal VZA about the subsatellite point are easily identifiable. The gray concave lines in all panels of Fig. A1 indicate lines of equal *Aqua* MODIS and *MTSAT-2* VZA (within 5°), and resemble the GEO-MetOp collocations in Hewison et al. (2013, their Fig. 1). The SZA are nearly identical because only images coincident within 15 min are used. East of the MODIS orbit, the RAA is in backscatter (>90°) conditions, whereas on the western side of the orbit forward scatter (<90°) conditions exist (i.e., the sun's direction is west of the *Aqua* orbit in this reference frame). For GEOs, most of the image is located in backscatter conditions.

Figure A1 RAA plots show three angular matching thresholds. The first level shows locations for ΔVZA and

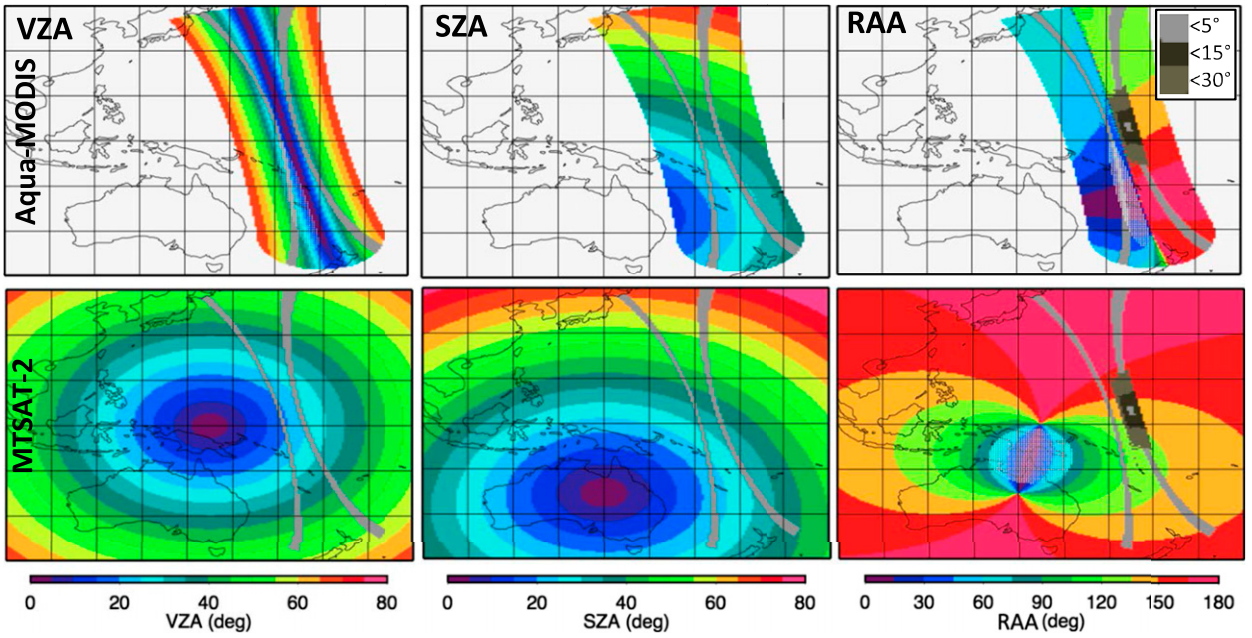

FIG. A1. The *Aqua* MODIS and *MTSAT-2* VZA, SZA, and RAA plotted on a 0.5° × 0.5° latitude by longitude grid for 0244 UTC 2 Jan 2013. The gray concave lines in all panels denote the *Aqua* and *MTSAT-2* matched view within 5° VZAs. The legend indicates three angular matching thresholds, e.g., <5° refers to where the VZA and RAA are both within 5°.

ΔRAA < 5°. The second and third levels are limited to ΔVZA and ΔRAA < 15°, and ΔVZA and ΔRAA < 30°, respectively. The MODIS VZA must also be <40°. Note the very small region for the most restrictive angular thresholds. As the angular matching is relaxed, the region extends mostly in the along-track direction. Figure A2 shows a case where the ray-matched region occurs in both the forward scatter and backscatter conditions, for which the forward condition encompasses a high probability of sun glint for both *MTSAT-2* and MODIS. The *MTSAT-2* angles were computed as if the image was instantaneously scanned at 0421 UTC

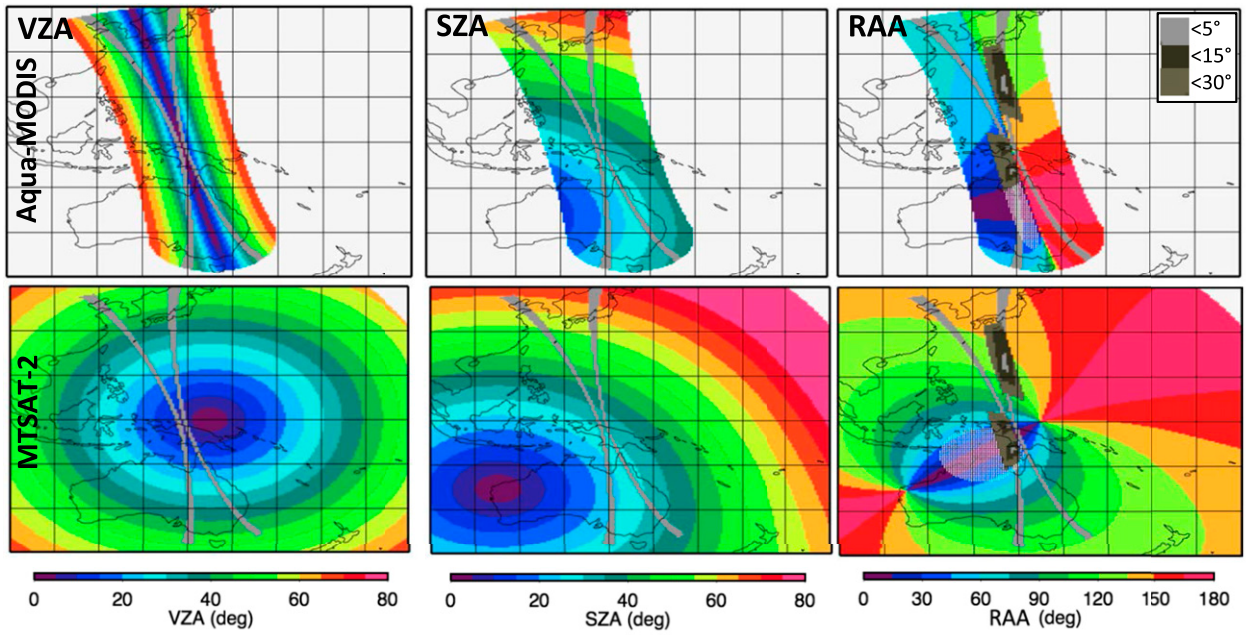

FIG. A2. As in Fig. A1, but at 0421 UTC 2 Jan 2013.

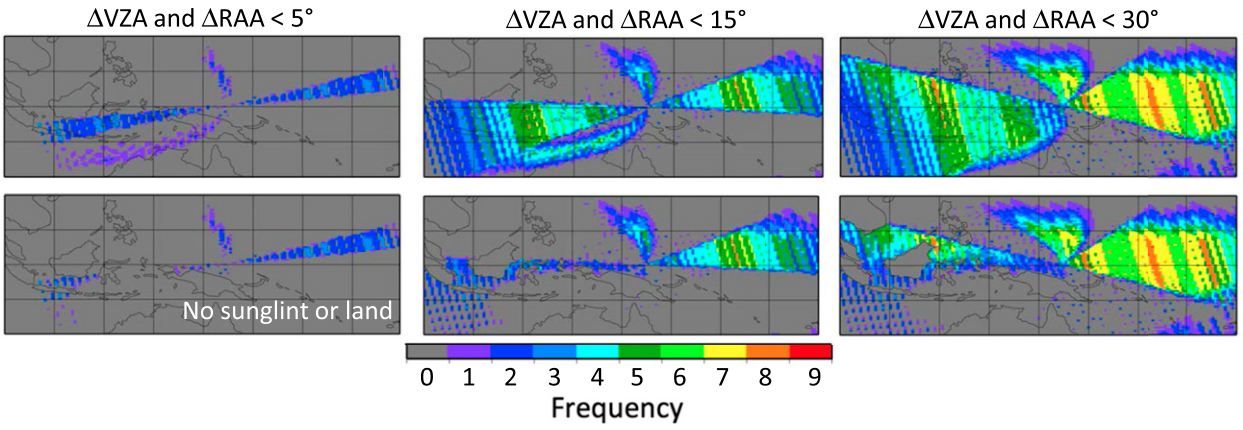

FIG. A3. (top) January 2011 *MTSAT-2*/*Aqua* MODIS 0.5° × 0.5° latitude by longitude gridded coincident ray-matching frequency. (bottom) As in (top), but excludes sun-glint conditions and land regions.

2 January 2013—the equator crossing time of the *Aqua*. Typically, the *Aqua* orbit transects the GEO domain 3 or 4 times during daylight hours, with orbital intersects ~25° apart in longitude.

Figure A3 summarizes the ray-matching frequency for January 2011 for the three angular matching thresholds. Both the sampling frequency and the extent of ray-matched regions increase significantly as the angular restrictions are relaxed. The bottom panels in Fig. A3 have excluded areas of sun glint and land regions in the ray-matching frequency plots, which therefore have reduced the sampling frequency, mainly in the southwest quadrant of the grid. Figure A4 displays the ray-matching frequency for the four seasonal months during 2011. The ray-matched bow tie domain located in the northeast and southwest quadrants are present in all months. The other ray-matched domains are season specific. Removing sun glint significantly reduces the sampling frequency on the west side of the *MTSAT-2* subsatellite position. This sampling frequency pattern

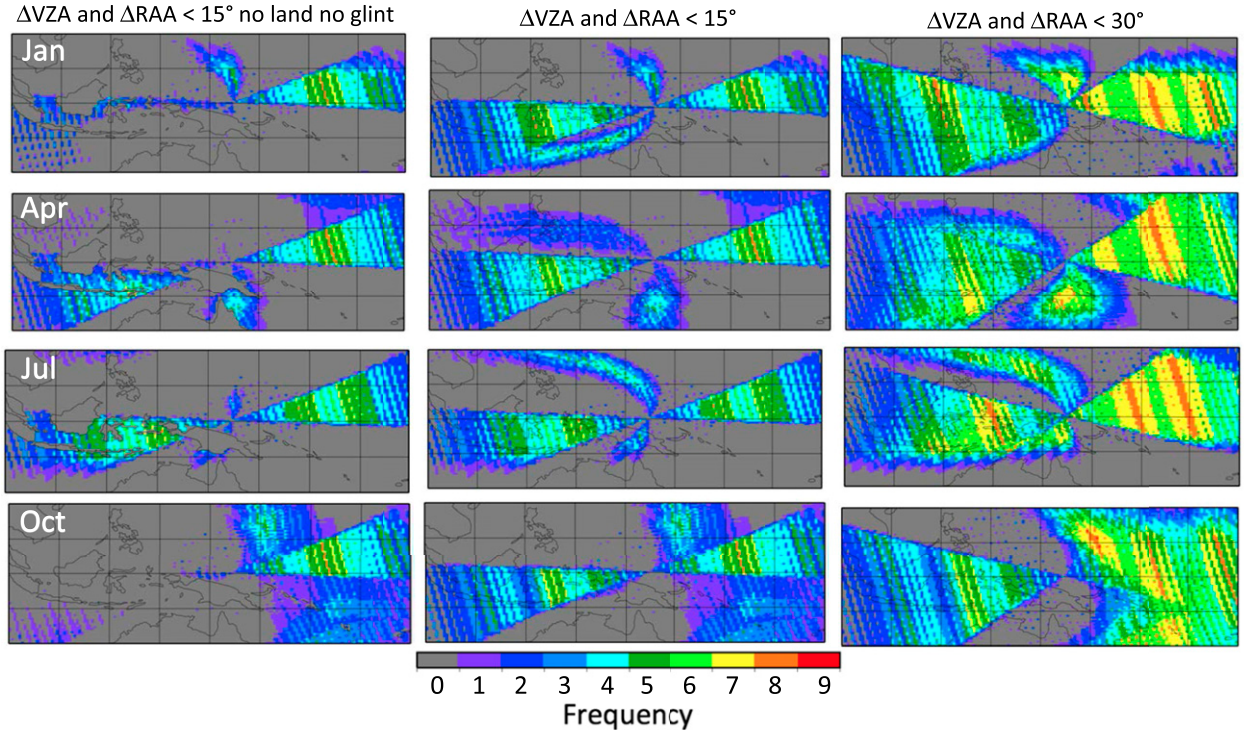

FIG. A4. The 2011 seasonal month *MTSAT-2*/*Aqua* MODIS 0.5° × 0.5° latitude by longitude gridded coincident ray-matching frequency.

should be the same for all GEO sensors utilizing *Aqua* MODIS ray matching. However, the location of land regions will be GEO specific. An advantage of DCC over ATO ray matching is the fact that neither areas of sun glint nor land regions need to be excluded.

REFERENCES

Acarreta, J. R., and P. Stammes, 2005: Calibration comparison between SCIAMACHY and MERIS onboard ENVISAT. *Geosci. Remote Sens. Lett.*, **2**, 31–35, doi:10.1109/LGRS.2004.838348.

Ayers, J. K., L. Nguyen, W. L. Smith Jr., and P. Minnis, 1998: Calibration of geostationary satellite imager data for ARM using AVHRR. *Proceedings of the Eighth Atmospheric Radiation Measurement (ARM) Science Team Meeting*, U.S. Dept. of Energy DOE/ER-0738, UC-402, 45–49. [Available online at http://www.arm.gov/publications/proceedings/conf08/extended_abs/ayers_jk.pdf.]

Berendes, T. A., J. R. Mecikalski, W. M. MacKenzie Jr., K. M. Bedka, and U. S. Nair, 2008: Convective cloud identification and classification in daytime satellite imagery using standard deviation limited adaptive clustering. *J. Geophys. Res.*, **113**, D20207, doi:10.1029/2008JD010287.

Bhatt, R., D. R. Doelling, D. Morstad, B. R. Scarino, and A. Gopalan, 2014: Desert-based absolute calibration of successive geostationary visible sensors using a daily exoatmospheric radiance model. *IEEE Trans. Geosci. Remote Sens.*, **52**, 3670–3682, doi:10.1109/TGRS.2013.2274594.

Brest, C. L., W. B. Rossow, and M. D. Roiter, 1997: Update of radiance calibrations for ISCCP. *J. Atmos. Oceanic Technol.*, **14**, 1091–1109, doi:10.1175/1520-0426(1997)014<1091:UORCFI>2.0.CO;2.

Chander, G., N. Mishra, D. L. Helder, D. B. Aaron, A. Angal, T. Choi, X. Xiong, and D. R. Doelling, 2013: Applications of spectral band adjustment factors (SBAF) for cross-calibration. *IEEE Trans. Geosci. Remote Sens.*, **51**, 1267–1281, doi:10.1109/TGRS.2012.2228007.

Desormeaux, Y., W. B. Rossow, C. L. Brest, and G. G. Campbell, 1993: Normalization and calibration of geostationary satellite radiances for ISCCP. *J. Atmos. Oceanic Technol.*, **10**, 304–325, doi:10.1175/1520-0426(1993)010<0304:NACOGS>2.0.CO;2.

Doelling, D. R., P. Minnis, and L. Nguyen, 2004: Calibration comparisons between SEVIRI, MODIS, and GOES data. *Proceedings of the Second MSG RAO Workshop*, H. Lacoste, Ed., ESA Publ. SP-582, 149–154.

——, D. P. Garber, L. A. Avey, L. Nguyen, and P. Minnis, 2007: The calibration of AVHRR visible dual gain using Meteosat-8 for NOAA-16 to 18. *Atmospheric and Environmental Remote Sensing Data Processing and Utilization III: Readiness for GEOSS*, M. D. Goldberg et al., Eds., International Society for Optical Engineering (SPIE Proceedings, Vol. 6684), 668409, doi:10.1117/12.736080.

——, R. Bhatt, D. Morstad, and B. Scarino, 2011: Algorithm theoretical basis document (ATBD) for ray-matching technique of calibrating GEO sensors with Aqua-MODIS for GSICS. WMO, 10 pp. [Available online at http://gsics.atmos.umd.edu/pub/Development/AtbdCentral/GSICS_ATBD_DCC_NASA_2011_09.pdf.]

——, C. Lukashin, P. Minnis, B. Scarino, and D. Morstad, 2012: Spectral reflectance corrections for satellite intercalibrations using SCIAMACHY data. *Geosci. Remote Sens. Lett.*, **9**, 119–123, doi:10.1109/LGRS.2011.2161751.

——, and Coauthors, 2013a: Geostationary enhanced temporal interpolation for CERES flux products. *J. Atmos. Oceanic Technol.*, **30**, 1072–1090, doi:10.1175/JTECH-D-12-00136.1.

——, D. Morstad, B. R. Scarino, R. Bhatt, and A. Gopalan, 2013b: The characterization of deep convective clouds as an invariant calibration target and as a visible calibration technique. *IEEE Trans. Geosci. Remote Sens.*, **51**, 1147–1159, doi:10.1109/TGRS.2012.2225066.

——, B. R. Scarino, D. Morstad, A. Gopalan, R. Bhatt, C. Lukashin, and P. Minnis, 2013c: The intercalibration of geostationary visible imagers using operational hyperspectral SCIAMACHY radiances. *IEEE Trans. Geosci. Remote Sens.*, **51**, 1245–1254, doi:10.1109/TGRS.2012.2227760.

——, and Coauthors, 2015a: MTSAT-1R visible imager point spread correction function, Part I: The need for, validation of, and calibration with. *IEEE Trans. Geosci. Remote Sens.*, **53**, 1513–1526, doi:10.1109/TGRS.2014.2344678.

——, A. Wu, X. Xiong, B. R. Scarino, R. Bhatt, C. O. Haney, D. Morstad, and A. Gopalan, 2015b: The radiometric stability and scaling of collection 6 Terra- and Aqua-MODIS VIS, NIR, and SWIR spectral bands. *IEEE Trans. Geosci. Remote Sens.*, **53**, 4520–4535, doi:10.1109/TGRS.2015.2400928.

Fougnie, B., and R. Bach, 2009: Monitoring of radiometric sensitivity changes of space sensors using deep convective clouds: Operational application to PARASOL. *IEEE Trans. Geosci. Remote Sens.*, **47**, 851–861, doi:10.1109/TGRS.2008.2005634.

Govaerts, Y., and M. Clerici, 2004: MSG-1/SEVIRI solar channels calibration commissioning activity report. Version 1.0, EUMETSAT Rep. EUM/MSG/TEN/04/0024, 35 pp. [Available online at http://www.eumetsat.int/website/wcm/idc/idcplg?IdcService=GET_FILE&dDocName=PDF_TEN_040024_SEVIRI-SOLCALIB&RevisionSelectionMethod=LatestReleased&Rendition=Web.]

Guenther, B., X. Xiong, V. V. Salomonson, W. L. Barnes, and J. Young, 2002: On-orbit performance of the Earth Observing System Moderate Resolution Imaging Spectroradiometer; first year of data. *Remote Sens. Environ.*, **83**, 16–30, doi:10.1016/S0034-4257(02)00097-4.

Ham, S.-H., and B.-J. Sohn, 2010: Assessment of the calibration performance of satellite visible channels using cloud targets: Application to Meteosat-8/9 and MTSAT-1R. *Atmos. Chem. Phys.*, **10**, 11 131–11 149, doi:10.5194/acp-10-11131-2010.

Heidinger, A. K., W. C. Straka III, C. C. Molling, J. T. Sullivan, and X. Wu, 2010: Deriving an inter-sensor consistent calibration for the AVHRR solar reflectance data record. *Int. J. Remote Sens.*, **31**, 6493–6517, doi:10.1080/01431161.2010.496472.

Hennon, C. C., C. N. Helms, K. R. Knapp, and A. R. Bowen, 2011: An objective algorithm for detecting and tracking tropical cloud clusters: Implications for tropical cyclogenesis prediction. *J. Atmos. Oceanic Technol.*, **28**, 1007–1018, doi:10.1175/2010JTECHA1522.1.

Henry, P., G. Chander, B. Fougnie, C. Thomas, and X. Xiong, 2013: Assessment of spectral band impact on intercalibration over desert sites using simulation based on EO-1 Hyperion data. *IEEE Trans. Geosci. Remote Sens.*, **51**, 1297–1308, doi:10.1109/TGRS.2012.2228210.

Hewison, T. J., X. Wu, F. Yu, Y. Tahara, X. Hu, D. Kim, and M. Koenig, 2013: GSICS inter-calibration of infrared channels of geostationary imagers using Metop/IASI. *IEEE Trans. Geosci. Remote Sens.*, **51**, 1160–1170, doi:10.1109/TGRS.2013.2238544.

Hong, G., G. Heygster, J. Notholt, and S. A. Buehler, 2008: Interannual to diurnal variations in tropical and subtropical deep

convective clouds and convective overshooting from seven years of AMSU-B measurements. *J. Climate*, **21**, 4168–4189, doi:10.1175/2008JCLI1911.1.

Ignatov, A., C. Cao, J. Sullivan, R. Levin, X. Wu, and R. Galvin, 2005: The usefulness of in-flight measurements of space count to improve calibration of the AVHRR solar reflectance bands. *J. Atmos. Oceanic Technol.*, **22**, 180–200, doi:10.1175/JTECH-1691.1.

Inamdar, A. K., and K. R. Knapp, 2015: Intercomparison of independent calibration techniques applied to the visible channel of the ISCCP B1 data. *J. Atmos. Oceanic Technol.*, **32**, 1225–1240, doi:10.1175/JTECH-D-14-00040.1.

Jourdan, O., A. A. Kikhanovsky, and J. P. Burrows, 2007: Calibration of SCIAMACHY using AATSR top-of-atmosphere reflectance over a hurricane. *Geosci. Remote Sens. Lett.*, **4**, 8–12, doi:10.1109/LGRS.2006.881726.

Khlopenkov, K. V., D. R. Doelling, and A. Okuyama, 2015: MTSAT-1R visible imager point spread function correction, Part II: Theory. *IEEE Trans. Geosci. Remote Sens.*, **53**, 1504–1512, doi:10.1109/TGRS.2014.2344627.

Kim, B.-R., S.-H. Ham, D. Kim, and B.-J. Sohn, 2014: Post-flight radiometric calibration of the Korean geostationary satellite COMS meteorological imager. *Asia-Pac. J. Atmospheric Sci.*, **50**, 201–210, doi:10.1007/s13143-014-0008-7.

Koelemeijer, R. B. A., P. Stamnes, and P. D. Watts, 1998: Comparison of visible calibrations of GOME and ATSR-2. *Remote Sens. Environ.*, **63**, 279–288, doi:10.1016/S0034-4257(97)00161-2.

LaFrance, B., O. Hagolle, B. Bonnel, Y. Fouquart, and G. Brogniez, 2002: Interband calibration over clouds for POLDER space sensor. *IEEE Trans. Geosci. Remote Sens.*, **40**, 131–142, doi:10.1109/36.981355.

Lazzara, M. A., and Coauthors, 1999: The Man computer Interactive Data Access System: 25 years of interactive processing. *Bull. Amer. Meteor. Soc.*, **80**, 271–284, doi:10.1175/1520-0477(1999)080<0271:TMCIDA>2.0.CO;2.

Le Marshall, J. F., J. J. Simpson, and Z. Jin, 1999: Satellite calibration using a collocated nadir observation technique: Theoretical basis and application to the GMS-5 Pathfinder benchmark period. *IEEE Trans. Geosci. Remote Sens.*, **37**, 499–507, doi:10.1109/36.739100.

Meirink, J. F., R. A. Roebeling, and P. Stammes, 2013: Inter-calibration of polar imager solar channels using SEVIRI. *Atmos. Meas. Tech.*, **6**, 2495–2508, doi:10.5194/amt-6-2495-2013.

Minnis, P., and E. F. Harrison, 1984: Diurnal variability of regional cloud and clear-sky radiative parameters derived from GOES data. Part III: November 1978 radiative parameters. *J. Climate Appl. Meteor.*, **23**, 1032–1051, doi:10.1175/1520-0450(1984)023<1032:DVORCA>2.0.CO;2.

——, W. L. Smith Jr., D. P. Garber, J. K. Ayers, and D. R. Doelling, 1994: Cloud properties derived from GOES-7 for spring 1994 ARM intensive observing period using version 1.0.0 of ARM satellite data analysis program. NASA Reference Publ. NASA RP-1366, 59 pp.

——, L. Nguyen, D. R. Doelling, D. F. Young, W. F. Miller, and D. P. Kratz, 2002: Rapid calibration of operational and research meteorological satellite imagers. Part I: Evaluation of research satellite visible channels as references. *J. Atmos. Oceanic Technol.*, **19**, 1233–1249, doi:10.1175/1520-0426(2002)019<1233:RCOOAR>2.0.CO;2.

Morstad, D. L., D. R. Doelling, R. Bhatt, and B. Scarino, 2011: The CERES calibration strategy of the geostationary visible channels for CERES cloud and flux products. *Earth Observing Systems XVI*, J. J. Butler, X. Xiong, and X. Gu, Eds., International Society for Optical Engineering (SPIE Proceedings, Vol. 8153), 815316, doi:10.1117/12.894650.

Nagaraja Rao, C. R., N. Zhang, and J. T. Sullivan, 2001: Intercalibration of meteorological satellite sensors in the visible and near-infrared. *Adv. Space Res.*, **28**, 3–10, doi:10.1016/S0273-1177(01)00262-9.

Nguyen, L., P. Minnis, J. K. Ayers, W. L. Smith Jr., and S. P. Ho, 1999: Intercalibration of geostationary and polar satellite data using AVHRR, VIRS, and ATSR-2 data. *Proc. 10th Conf. on Atmospheric Radiation*, Madison, WI, Amer. Meteor. Soc., 405–408.

——, ——, ——, and D. R. Doelling, 2001: Intercalibration of meteorological satellite imagers using VIRS, ATSR-2, and MODIS. *Proc. 11th Conf. on Satellite Meteorology and Oceanography*, Madison, WI, Amer. Meteor. Soc., P4.3. [Available online at https://ams.confex.com/ams/11satellite/techprogram/paper_24406.htm.]

——, D. R. Doelling, P. Minnis, and J. K. Ayers, 2004: Rapid technique to cross-calibrate satellite imager visible channels. *Earth Observing Systems IX*, W. L. Barnes and J. J. Butler, Eds., International Society for Optical Engineering (SPIE Proceedings, Vol. 5542), 227, doi:10.1117/12.560138.

Okuyama, A., 2011: Outlined algorithm theoretical basis for MTSAT visible calibration for GSICS (liquid cloud method). GSICS Algorithm Theoretical Basis Doc., 6 pp. [Available online at http://gsics.atmos.umd.edu/pub/Development/AtbdCentral/MTSAT_vis_vicarious_calibration_outline.pdf.]

Rutan, D., S. Kato, D. Doelling, F. Rose, L. Nguyen, T. Caldwell, and N. Loeb, 2015: CERES synoptic product: Methodology and validation of surface radiant flux. *J. Atmos. Oceanic Technol.*, **32**, 1121–1143, doi:10.1175/JTECH-D-14-00165.1.

Scarino, B. R., D. R. Doelling, D. L. Morstad, R. Bhatt, A. Gopalan, C. Lukashin, and P. Minnis, 2012: Using SCIAMACHY to improve corrections for spectral band differences when transferring calibration between visible sensors. *Earth Observing Systems XVII*, J. J. Butler, X. Xiong, and X. Gu, Eds., International Society for Optical Engineering (SPIE Proceedings, Vol. 8510), 85100Q, doi:10.1117/12.929767.

——, ——, P. Minnis, A. Gopalan, T. Chee, R. Bhatt, C. Lukashin, and C. Haney, 2016: A web-based tool for calculating spectral band difference adjustment factors derived from SCIAMACHY hyperspectral data. *IEEE Trans. Geosci. Remote Sens.*, **54**, 2529–2542, doi:10.1109/TGRS.2015.2502904.

Skupin, J., S. Noël, M. W. Wuttke, M. Gottwald, H. Bovensmann, M. Weber, and J. P. Burrows, 2005: SCIAMACHY solar irradiance observation in the spectral range from 240 to 2380 nm. *Adv. Space Res.*, **35**, 370–375, doi:10.1016/j.asr.2005.03.036.

Slater, P. N., S. F. Biggar, R. G. Holm, R. D. Jackson, Y. Moa, M. S. Moran, J. M. Palmer, and B. Yuan, 1987: Reflectance- and radiance-based methods for the in-flight absolute calibration of multispectral sensors. *Remote Sens. Environ.*, **22**, 11–37, doi:10.1016/0034-4257(87)90026-5.

Teillet, P. M., G. Fedosejevs, R. P. Gauthier, N. T. O'Niell, K. J. Thome, S. F. Biggar, H. Ripley, and A. Meygret, 2001: A generalized approach to the vicarious calibration of multiple Earth observation sensors using hyperspectral data. *Remote Sens. Environ.*, **77**, 304–327, doi:10.1016/S0034-4257(01)00211-5.

Vermote, E., and Y. J. Kaufman, 1995: Absolute calibration of AVHRR visible and near-infrared channels using ocean and

cloud views. *Int. J. Remote Sens.*, **16**, 2317–2340, doi:10.1080/01431169508954561.

Weinreb, M., M. Jamieson, N. Fulton, Y. Chen, J.-X. Johnson, J. Bremer, C. Smith, and J. Baucom, 1997: Operational calibration of Geostationary Operational Environmental Satellite-8 and -9 imagers and sounders. *Appl. Opt.*, **36**, 6895–6904, doi:10.1364/AO.36.006895.

Wielicki, B. A., B. R. Barkstrom, E. F. Harrison, R. B. Lee III, G. L. Smith, and J. E. Cooper, 1996: Clouds and the Earth's Radiant Energy System (CERES): An Earth Observing System experiment. *Bull. Amer. Meteor. Soc.*, **77**, 853–868, doi:10.1175/1520-0477(1996)077<0853:CATERE>2.0.CO;2.

——, D. R. Doelling, D. F. Young, N. G. Loeb, D. P. Garber, and D. G. MacDonnell, 2008: Climate quality broadband and narrowband solar reflected radiance calibration between sensors in orbit. *2008 IEEE International Geoscience and Remote Sensing Symposium: Proceedings*, IEEE, I-257–I-260, doi:10.1109/IGARSS.2008.4778842.

Wu, A., X. Xiong, D. R. Doelling, D. Morstad, A. Angal, and R. Bhatt, 2013: Characterization of Terra and Aqua MODIS VIS, NIR, and SWIR spectral bands' calibration stability. *IEEE Trans. Geosci. Remote Sens.*, **51**, 4330–4338, doi:10.1109/TGRS.2012.2226588.

Wu, X., H. Qian, F. Yu, and T. Beck, 2011: Vicarious calibration of GOES visible channel using GOME-2. *2011 IEEE International Geoscience and Remote Sensing Symposium: Proceedings*, IEEE, 1033–1035, doi:10.1109/IGARSS.2011.6049310.